Challenging microscopic structure and reaction models for nucleon scattering off nuclei in the $A = 208$ mass region

M. Dupuis,* G. Haouat, J.-P. Delaroche, E. Bauge, and J. Lachkar†
CEA, DAM, DIF, F-91297 Arpajon, France

(Received 27 February 2019; published 11 October 2019)

We present a microscopic description of neutron and proton elastic and inelastic scattering off ^{206,207,208}Pb and ^{209}Bi together with new medium-energy (7.5–15.5 MeV) neutron elastic and inelastic scattering measurements for various low-energy levels. The Jeukenne, Lejeune, Mahaux (JLM) semimicroscopic folding model provides the relevant optical and transition potentials used to calculate the elastic and inelastic cross sections. Rearrangement corrections that account for proton and neutron density variations during the transition are considered. The nuclear diagonal and transition densities are calculated from a (quasiparticle) random phase approximation [(Q)RPA] structure model implemented with the Gogny D1S interaction. Calculated differential elastic and inelastic cross sections are mostly in very good agreement with available data. Predicted nuclear structure properties as well as scattering calculations and measurements for the yrast quadrupole excitation in ^{206}Pb are carefully discussed. The rearrangement corrections to inelastic scattering form factors are shown to reduce medium energy nucleon inelastic cross section by up to 55%. The magnitude of these corrections changes depending on the probe, incident energy, multipolarity, and nature of the transitions considered. The combined analysis of nuclear structure properties and those for nucleon scattering cross sections measured previously over a range of incident energies provides stringent tests of present microscopic models and helps distinguish those scattering data which most likely call for revision.

DOI: 10.1103/PhysRevC.100.044607

I. INTRODUCTION

Direct elastic and inelastic nucleon scattering mechanisms are qualitatively and mostly quantitatively well understood [1]. However, when browsing the tremendous number of published studies on this subject, one can observe discrepancies between calculations and measured cross sections, even for stable nuclei. They could be attributed to inaccuracies of the modeling, but the analysis of inelastic cross sections for various energy, isotopes, and levels sometimes reveals inconsistent data sets. Recently, systematic statistical analyses of the EXFOR database [2] have been performed to identify erroneous data sets for various reactions [3,4], especially through comparisons with calculations performed with the nuclear reaction code TALYS [5]. This emphasizes that new precise data for nucleon scattering, even on stable nuclei, are needed to refine nuclear reaction database and nuclear reaction models.

Nowadays, microscopic models are routinely used to describe nucleon-induced reactions. The microscopic nucleon-nucleus optical model potential (OMP) of Jeukenne, Lejeune, and Mahaux (JLM) [6] has provided overall good agreement with elastic and quasielastic scattering measurements over a broad range of energy and mass [7–11]. Agreements of similar quality have been achieved in extensions of the JLM model to nucleon inelastic scattering analyses conducted within the distorted wave Born approximation (DWBA) for spherical targets [12], and within the coupled channel formalism for deformed nuclei, from ^{30}S to ^{238}U [13–17]. These previous works used mean-field and beyond-mean-field radial densities as input to the folding model. The JLM folding model is a powerful tool to challenge nuclear structure model and extract nuclear structure information from new measured cross sections as shown in recently reported studies for halo nuclei [18] and radioactive nuclei [19,20]. Early studies have shown that including rearrangements terms in microscopic modeling of inelastic scattering strongly impacts predictions [21–23].

In the present work, new neutron elastic and inelastic scattering measurement are reported for the four target ^{206,207,208}Pb and ^{209}Bi. These measurements were carried out about three decades ago [24,25], and most of the data obtained at that time have not been published yet. Elastic and inelastic scattering differential cross sections are determined within the JLM folding model. Inelastic cross sections are obtained through the DWBA formalism. Expressions of the optical and transition potentials to be used in the calculations of elastic and inelastic scattering, based on a local-density approximation (LDA), are detailed, including rearrangement (i.e., dynamical) corrections, that were ignored in a previous analysis of selected data for (n, n') scattering off ^{208}Pb [26]. Nuclear structure calculations providing needed matter densities are performed within the (quasiparticle) random phase approximation [(Q)RPA] model implemented with the D1S Gogny interaction [17,27,28]. All neutron data in the energy range 4–26 MeV for the ^{206,207,208}Pb and ^{209}Bi targets are analyzed to demonstrate the coherence between the present new data set and existing measurements, to show the predictive power of our microscopic model, and to eventually identify

*marc.dupuis@cea.fr
†Present address: CEA DEN Saclay, France.

 ©2019 American Physical Society

questionable data sets. The impact of rearrangement corrections is analyzed for both neutron and proton inelastic scattering to various levels. Results from our microscopic model and experimental data are also compared to calculations from phenomenological optical potential and the collective model for inelastic scattering.

Section II describes the experimental system, detailing the primary-neutron production method, the data acquisition system, the sample properties, and the measurements. Section III describes the JLM-B folding model, including rearrangement terms. The (Q)RPA nuclear structure method, that provides the necessary ingredients to the folding model, is summarized in Sec. IV, where predicted excitation functions, nuclear densities, and excitation energies are compared to available structure data. Section V reviews the main features of the collective model for nucleon inelastic scattering, and then Sec. VI reviews the weak-coupling approximation for odd targets. In Sec. VII, calculated differential cross sections are compared to all the available neutron scattering experimental data in the 4- to 26-MeV range for the four studied isotopes, including the new data. The impact of rearrangement corrections on inelastic scattering cross sections is also illustrated. A specific discussion is dedicated to the modeling of the ^{206}Pb$(n, n')2_1^+$ reactions. A summary of and conclusion to this work are provided in Sec. VIII.

II. EXPERIMENTAL METHOD AND RESULTS

The differential cross sections were measured using the neutron time-of-flight (TOF) facility of the CEA DAM Ile-de-France tandem accelerator laboratory. This facility, consisting of a multidetector spectrometer installed in a large-size "neutron hall," had been especially designed to perform fast-neutron scattering measurements with a high energy resolution in a low background environment. The "hall" was a rectangular building 36 m long, 26 m side, and 8 m high with thin roof and walls. The beam line entered parallel to the long axis but off center to permit flight paths for neutron detection up to at least 18 m at all angles between 0 and 160°. It was installed ≈1.7 m above floor level and terminated over the center of a cylindrical "pit" in the floor, of 5 m radius and 3 m deep. The neutron source was mounted at the end of the beam extension, close to the center of the pit [29]. This geometry contributed to greatly reduce time-independent background of neutrons and γ rays. The characteristics of the neutron TOF facility have been presented in detail previously [30–32] and thus the description given below will emphasize those features peculiar to the measurements presented below.

A. Experimental systems

1. Primary-neutron production

The experimental procedure had been planned as follows. A pulsed beam of deuterons delivered by the EN (7 MV maximum voltage) tandem Van de Graaff accelerator was incident on a deuterium gas cell to produce neutrons by the ^{2}H$(d, n)^3$He reaction. The choice of this neutron-producing reaction will be discussed below.

The neutrons were then scattered from small samples of Bi and Pb into an array of four detectors. Scattered neutron energies were determined via TOF techniques. The deuteron beam delivered by an ion injector, operated at a 120-kV pre-injection voltage, was chopped at a repetition rate of 2.5 MHz and bunched into bursts, with a full width at half maximum (FWHM) of 1.3 ns duration before entering the accelerator. The emerging high-energy pulsed beam was momentum analyzed in a first 45° magnetic dipole deflecting to the right. It entered next a postaccelerator bunching system consisting of a second 45° magnetic dipole, also deflecting to the right, and a 19-m-long drift space, and finally terminated in the deuterium gas target. A well-designed capacitive beam pick-off was placed in front of the target, at about 1 m from it, to accurately sense the arrival of beam pulses; this detector was of particular importance to perform precise TOF measurements. Deuteron beams were accelerated at energies ranging from 4.5 to 12.6 MeV. By adjusting the energy distribution along the beam burst at the entrance of the postaccelerator bunching system, pulse widths as short as 1.0 ns at the target location were routinely achieved. This parameter was regularly checked, during data-collection runs, by TOF measurement of the prompt γ rays from deuteron-induced reactions in the beam stop at the end of the gas target. During the experiment, the average beam current on the target varied typically from 3.0 to 5.5 μA with increasing energy of the deuterons.

The deuteron beam entered the deuterium-gas target to produce, via the ^{2}H$(d, n)^3$He reaction, monoenergetic neutrons in the 7.5- to 15.5-MeV energy range. Design and operation of the gas target have been presented in detail in previous publications [30–32]. For the work presented here, it was filled at a pressure of approximately 1.5 bars, which allowed long-term operation for the target with deuteron beams of 3-mm-diameter spot and up to 7-μA mean current. The energy spread of the monokinetic neutrons incident on the scattering samples, which was due to deuteron-beam energy dispersion, straggling in the entrance foil, energy-loss variation along the target cell, and solid-angle opening of the samples at the target location, was estimated to be roughly constant from 7.5 to 15.5 MeV and equal to 150 keV FWHM. The neutron flux on the sample was evaluated to vary from 3 to 8×10^8 neutrons/sr s from 7.5 to 15.5 MeV.

The incident-neutron spectrum was not purely monoenergetic since, above a deuteron energy threshold of 4.45 MeV, the ^{2}H$(d, np)^2$H breakup reaction gives rise to a wide-energy-spectrum neutron flux that increases with deuteron energy [31,33–36] and may be undesirable. However, the energy difference, at 0° with respect to the beam axis, between the monoenergetic neutrons and the most energetic neutrons of the breakup reaction is ≈7 MeV, large enough to enable scattering measurements for the ground states and excited states of at least up to 7 MeV energy.

2. Scattered-neutron spectrometry

The primary neutrons bombarded small right cylinders of lead and bismuth; each sample was placed, with its axis set vertically, symmetrically on the deuteron-beam line at a distance from the gas-cell center of roughly ten centimeters.

It was hung from a lightweight aluminum frame by means of thin stainless steel wires. At each sample interchange, the alignment of the sample on the beam axis and the distance from the cell to the sample were checked with telescopes. Precise values of the sizes and isotopic compositions of the samples as well as values of the cell-to-sample distance will be given further below in Sec. II A 4.

The scattered neutrons were detected by an array of four identical recoil-proton detectors placed in the horizontal plane containing the deuteron-beam axis and separated from each other by angular intervals of 20°. The scattering geometry and the detector shielding device have been described in previous publications [30–32,37].

The whole set of detector tanks, intermediate collimators, and shadow bars constituting the shielding device (Fig. 2 in Ref. [38]) was moved periodically to cover the entire angular range between 20° (15° for some measurements) and 160° in steps of 5°. Angular position of all the elements was determined with an accuracy of ±0.2°.

The flight path from the scattering sample to each detector was 8.00 m for all measurements; it was determined with an accuracy of ±2 cm. This flight-path length was fixed in accordance with the other experimental parameters, namely time and energy spreads of the incident neutrons at the sample location, sample dimensions, detector time, and energy resolutions, and time resolution of the data-acquisition electronic system, so as to achieve a scattered-neutron overall energy resolution of 240 keV FWHM at 7.5 MeV and increasing almost linearly with energy up to 380 keV FWHM at 15.5 MeV. This choice represented a satisfactory compromise between a comfortable counting rate and an overall time resolution sufficiently good to easily separate the scattered-neutron groups of interest in the TOF spectra.

During the scattering measurements, the primary neutron production was monitored continuously using two independent methods. In the first one, an auxiliary TOF detector, identical with the main detectors, counted the neutrons directly emitted by the gas target at a fixed angle of 55° on the opposite side of the beam line and at a distance of 8.00 m (Fig. 2 in Ref. [38]). In the second one, two surface-barrier diodes, each at 90° relative to the deuteron beam axis in the vertical plane, detected the protons produced by the ^{2}H$(d, p)^{3}$H reaction from the deuterium gas through windows in the target holder (Fig. 1 in Ref. [31]). Throughout the course of all the measurements, the proton- and neutron-monitor indications were consistent with each other to within 0.3%. Normalization of the yields of scattered neutrons to the yields of the neutron and proton monitors eliminated concern about deuteron-beam current integration and constancy of deuterium-gas pressure.

3. Data acquisition system

The measurements were performed using the standard TOF technique with conventional electronics. The electronic apparatus and the mode of operation have been detailed in Refs. [31,32,37]. Neutron γ-ray pulse shape discrimination was used to reject most of the γ-ray events induced in the scintillating detectors; this greatly contributed to reduce the time-independent background generated in the TOF spectra.

Flight time and recoil-proton pulse height for neutron events in each detector were recorded event by event in a two-parameter data acquisition system and stored on magnetic tape. This recording technique was very useful since in the off-line data reduction process the detector pulse height bias could be adjusted so as to minimize statistical uncertainties in the yields extracted from the TOF spectra. An on-line TOF spectrum was also generated for each detector for control during the experiment and was also stored on magnetic tape; the energy threshold for this spectrum was set at 30% of the primary-neutron energy. Threshold level and gain stability of the neutron detectors (including the neutron monitor), on which the overall detection efficiency depended, were checked with a Cs γ-ray source at regular time intervals and adjusted when necessary over the course of the experiment.

The fast timing signals from the detectors were gathered in a fast mixer and the corresponding linear signals were also gathered in a linear mixer, so as to reduce the number of electronic units and therefore to dispose of a more reliable electronic system. This arrangement was possible since the counting rate in each detector was not high enough to induce important dead time effects in the electronics. The identification of the detector which provided the neutron event was given by an auxiliary coincident pulse. The nominal time resolution of the whole electronic assembly was 1.0 ns, as checked by coincidence measurements with a ^{22}Na γ-ray source.

In addition, fast and linear outputs of the neutron and proton monitors were mixed with those of the neutron detectors. But, during the scattered-neutron acquisition runs, the counting rate of these monitors, viewing directly the neutron source, was much higher than that of the main detectors, which could distort the measurements. Therefore, the pulse rate from the monitors fast output was divided in fast scalers by appropriate numbers before entering the fast mixers, so as to obtain a reasonable counting rate, inducing negligible dead-time effects in the electronic apparatus.

4. Samples and measurements

The differential cross-section measurements reported here were obtained from two separate experiments. In the first one, referred to as Exp. 1, measurements were performed on a single sample of lead highly enriched in ^{208}Pb, at incident-neutron energies of 13.00 and 15.50 MeV. This sample, a right cylinder of solid pure metal, was borrowed from the Centre d'Études de Saclay; its dimensions and isotopic composition as well as the target-cell to sample distance are given in Table I. In the second experiment, achieved a few months later, measurements were performed on three samples of lead highly enriched respectively in ^{206}Pb, ^{207}Pb, and ^{208}Pb and one sample of natural bismuth at incident-neutron energies of 7.50, 9.50, 11.50, and 13.50 MeV. The samples were also in the form of right cylinders of solid pure metal; the ^{206}Pb and ^{207}Pb scatterers samples were available on free loan from Los Alamos National Laboratory, the ^{208}Pb one was available from Saclay, and the Bi cylinder was prepared in our laboratory.

TABLE I. Isotopic composition, dimensions, and mass of the samples, source-sample distance, and incident neutron energies for the two experiments performed. For Exp. 2, the source-sample distance and the incident-energy set are the same for the four targets.

Experiment	Sample (main isotope)	Isotopic composition (%)				Dimensions (mm)		Mass (M)		Dist. (mm)	E_n (MeV)
		206	207	208	209	Diam.	Height	M (g)	M (mol)		
Exp. 1	^{208}Pb	≈0.1	≈0.1	99.8		19.9	30.6	108.02	0.519	95.0	13.0, 15.5
	^{206}Pb	99.1	≈0.3	≈0.6		15.0	32.0	64.18	0.312		
	^{207}Pb	≈0.4	98.9	≈0.7		15.0	32.0	64.18	0.310		7.5, 9.5,
Exp. 2										110.0	
	^{208}Pb	12.5	1.0	86.5		15.0	31.0	62.18	0.299		11.5, 13.5
	^{209}Bi				100	16.0	32.0	62.99	0.301		

Characteristic parameters for this experiment, referred to as Exp. 2, are given in Table I.

Absolute differential cross-section values were obtained using the procedure described in Refs. [32,38], with considerably reduced relative and normalization uncertainties. Measurements for the ^{208}Pb sample, in Exp. 1, and for the ^{206}Pb, ^{207}Pb, ^{208}Pb, and ^{209}Bi samples, in Exp. 2, were taken in runs of 3 to 8 h, necessary to achieve a statistical precision better than 3% for elastic scattering at most angles. In addition, measurements without scattering sample were taken in order to subtract time-independent background and undesirable contributions in the TOF spectra.

5. Data reduction, corrections, and uncertainties

The TOF spectra were constructed off-line from event-mode tapes and then analyzed interactively. The spectra used for peak-yield analyses were created by subtracting the sample-out spectrum from the sample-in one, for each of the isotopically enriched samples. After background subtraction was achieved, which left clean spectra free of statistically significant distortions, net yields were obtained for isolated peaks both by direct summation of counts above a line fitted to the residual background in the neighborhood of the peaks and by fitting line shapes to the peaks to check for consistency of the yield extractions. The line profile, which was empirically determined, consisted of a Gaussian peak, representing the single scattering in the sample, to which an exponential tail was added on the low-energy side to take into account the multiple-scattering effects. For peaks too close to each other to be resolved completely, yields were obtained by an unfolding procedure using line profiles with shape parameters determined from analysis of the neighboring isolated peaks [32,39]. A typical TOF spectrum is presented in Fig. 1 (top panel) to illustrate the experimental energy resolution, the signal-to-noise ratio, and the good peak separation; an example of the peak-fitting procedure is shown on the bottom panel of Fig. 1.

The scattering yields thus obtained were rectified for dead time in the counting electronics, normalized for incident neutron fluence, with the aid of the 0°, no-sample runs, and for neutron detection efficiency (inelastic-scattering only), and corrected for finite-size effects of the neutron source at the sample to finally give the differential cross sections. The detailed expression for converting yields in the peaks to differential cross sections is given by Eq. (1) in Ref. [32]. This equation provides the cross-section values in the laboratory frame. They are then converted to values in the center-of-mass frame in order to be directly compared to theoretical model calculations. The finite-size effects include anisotropy of the neutron flux incident on the sample, angular resolution due to finite geometry of the neutron source, and the sample, incident

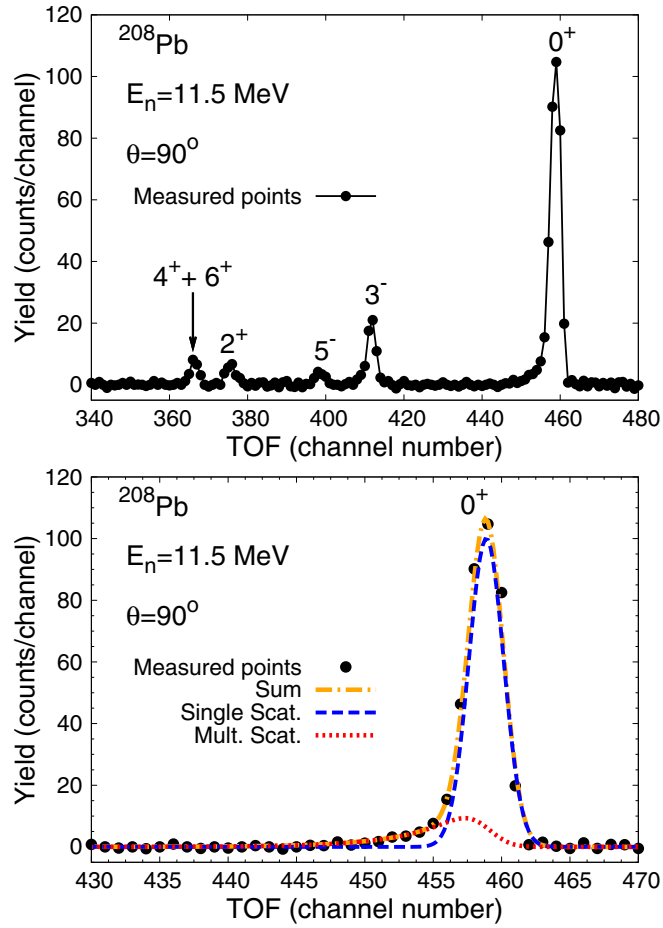

FIG. 1. Top panel: neutron TOF spectrum for 11.5-MeV neutrons scattered from ^{208}Pb at 90°. Values above the peaks indicate the spin and parity of the ground state (0^+) and excited levels. Bottom panel: enlargement of the elastic peak area with line-shape fitting of the elastic-scattering neutron peak.

TABLE II. Estimation of relative and normalization uncertainties for differential cross-section measurements.

Relative uncertainties (%)	
Counting statistic, background subtraction, unfolding, procedures	
Elastic scattering	2 to 15
Inelastic scattering	5 to 35
Flight path length	0.4 to 0.8
Sample corrections	1 to 3
Normalization uncertainties (%)	
Sample number of atoms	≈0.1
Monitor indications	1 to 2
Geometric factors	1 to 2
Detector relative efficiency (inelastic scattering only)	1 to 5

and scattered neutron attenuation by the sample, and multiple scattering in the sample. Corrections of all these effects were performed using the analytical method developed by Kinney to approximate, with a high level of accuracy, the results of Monte Carlo calculations [40].

The uncertainties assigned to the measured cross sections have been obtained by considering the derivative of Eq. (1) of Ref. [32]. They include relative uncertainties, which affect the reproducibility of measured data at each angle, and normalization uncertainties, which are common to a whole angular distribution. The relative errors arose mainly from counting statistics of the net yields of the TOF peaks and background subtraction, but these were minimized by using line-shape fitting procedures; they also arose, however, to a lesser extent, from measurement dispersion of flight-path length and scattering angle, and from sample-size effect corrections. The normalization or systematic errors were minimized in the measurements presented here since the incident and scattered neutron fluxes were measured with the same detector. These consisted of uncertainties in the estimation of the sample atom content, in the distances from source to sample and from source to 0° detector, in the indications of the neutron and proton monitors, in the evaluation of the correction factor for finite-geometry effects for the elastic-scattering cross sections, and in the determination of the detector relative efficiency for the inelastic-scattering cross sections. All of the uncertainties are listed in Table II. The relative uncertainties have been summed quadratically, the normalization uncertainties have been added arithmetically, and both uncertainties have been combined quadratically to yield the total uncertainty relevant to the measured cross section. To summarize, for elastic scattering, the relative errors range between 2%, mainly at forward angles, and 15%, essentially in the deep minima of the angular distributions, and the systematic errors are between 2 and 4%, while for inelastic scattering, the relative errors span from 5 to 35% and the systematic ones are between 3 and 9%. One can notice that, at least for elastic scattering, it could be possible to separate the relative contribution from the normalization one in the total uncertainties assigned to the differential cross sections.

B. Experimental results

1. New measured data

In Exp. 1, neutron differential cross-section measurements for the ^{208}Pb sample were completed at incident energies of 13.000 ± 0.052 and 15.500 ± 0.048 MeV, and, for each energy, at 30 angles from 15° to 160° in steps of 5°, with ten settings of the four-detector array. In Exp. 2, measurements for the ^{206}Pb, ^{207}Pb, ^{208}Pb, and ^{209}Bi samples were completed at incident energies of 7.500 ± 0.060, 9.500 ± 0.057, 11.500 ± 0.054, and 13.500 ± 0.051 MeV; for each sample and each energy, data were taken at 29 angles between 20° and 160° in steps of 5°, with nine settings of the detector array. In both experiments, the settings were arranged so that for each set of angles at least one previous data-collection angle was repeated; the goal of this procedure was to assure consistency of the data between the different angle sets. The large number of measurement angles was determined so as to yield a fairly precise description of the structure of the elastic-scattering angular distributions, especially those at high energies. Differential cross-sections extracted for the four isotopes are displayed in Figs. 2, 3 and 4 for elastic scattering, and in Figs. 5, 6, 7, and 8 for inelastic scattering. These are detailed as follows:

a. For the ^{206}Pb nucleus, cross sections were obtained for elastic scattering (0^+) and inelastic scattering on the 3^- (2.647 MeV) excited level at 7.5, 9.5, 11.5, and 13.5 MeV incident-neutron energies; cross sections were also obtained for the 2^+ (0.803 MeV) excited level at 11.5 and 13.5 MeV. The data are plotted further below in Fig. 2(b) for the ground state and in Figs. 5(b) and 5(c) for the two excited states.

b. For the odd nucleus ^{207}Pb, cross-section data were obtained for elastic scattering ($1/2^-$) and inelastic scattering on the unresolved ($5/2^+$; $7/2^+$) doublet centered around 2.640 MeV at energies of 7.5, 9.5, 11.5, and 13.5 MeV. Data are displayed respectively in Figs. 2(c), 6(a), and 6(b).

c. For the ^{208}Pb isotope, differential cross sections were obtained for elastic scattering (0^+) at incident-neutron energies of 7.5, 9.5, 11.5, 13.0, 13.5, and 15.5 MeV (Fig. 3), for inelastic scattering on the 3^- (2.614 MeV) level at 7.5, 9.5, 11.5, 13.0, 13.5, and 15.5 MeV, on the 5^- (3.198 MeV) level at 7.5, 9.5, 11.5, 13.0, and 13.5 MeV, and at 9.5, 11.5, and 13.5 MeV for the 2^+ (4.076 MeV) level and the unresolved (4^+; 6^+) levels centered around 4.380 MeV. Data for these excited states are plotted in Figs. 7 and 8.

d. For the other odd nucleus ^{209}Bi, data were obtained for elastic scattering ($9/2^-$) and inelastic scattering on the unresolved ($3/2^+$; $5/2^+$; $7/2^+$; $9/2^+$; $11/2^+$; $13/2^+$; $15/2^+$) multiplet centered around 2.600 MeV at energies of 7.5, 9.5, 11.5, and 13.5 MeV. Data are displayed respectively in Figs. 4 and 6.

As stated above, most of the data presented here have not been published. Only some measurements on ^{208}Pb were reported in a few works: Let us mention Refs. [12,41] for scattering from the ground state and the 3^- (2.614 MeV) excited state at 9.5 MeV, and Ref. [42] for elastic scattering cross sections at 7.5, 9.5, 11.5, and 13.5 MeV. These data were used to illustrate a semimicroscopic interpretation of elastic and inelastic scattering of nucleons by ^{208}Pb

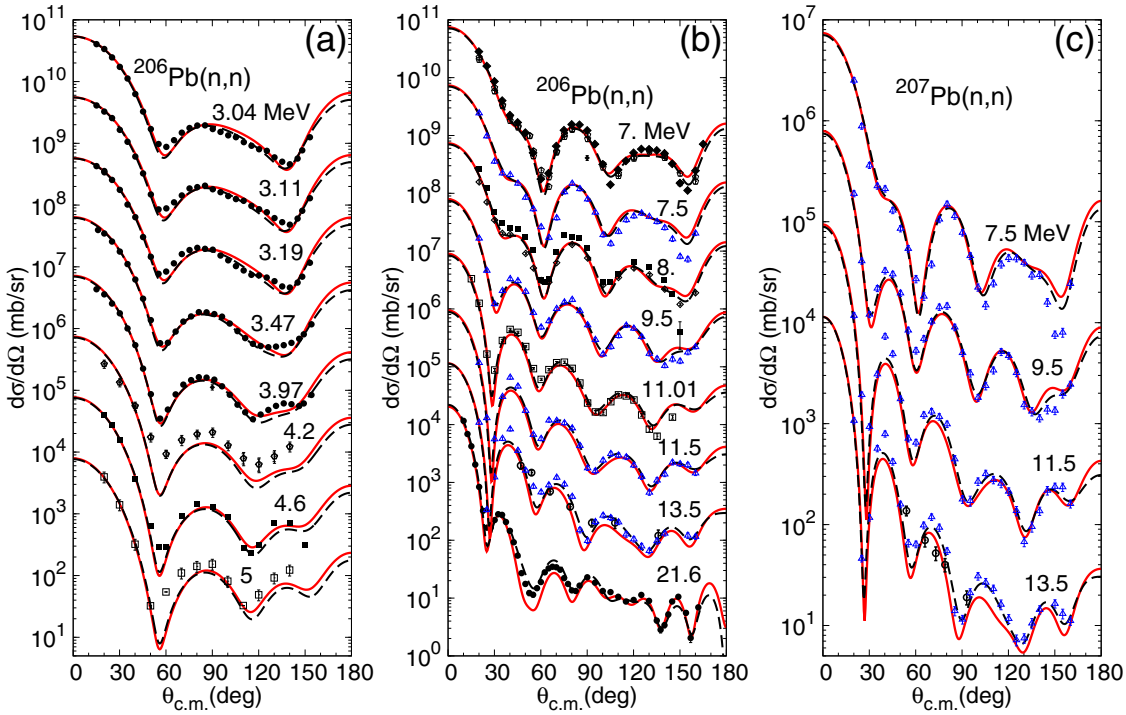

FIG. 2. Differential cross sections for neutron elastic scattering off ^{206}Pb [panels (a) and (b)] and ^{207}Pb [panel (c)] targets. Targets are indicated on each plot and incident energies above each curve. Cross sections are offset by factors of 10. Data from the experiment detailed in Sec. II are represented as open blue triangles. The various other symbols represent experimental values (see Refs. in Table III). JLM-B calculations with HFB matter densities are plotted as full red curves, calculations with the KD global optical potential as dash black curves. In panel (c), the data of Belovitskii *et al.* at 13.7 MeV [52] are represented as open black circles and plotted along with the calculations and the present data at 13.5 MeV.

[12,41] and to point out the limitations of the one-channel phenomenological optical potential in describing fast-neutron scattering by ^{208}Pb [42].

2. *Contribution to available database*

The present measurements add to the bulk of data available in the literature for elastic and inelastic scattering on ^{206}Pb, ^{207}Pb, ^{208}Pb, and ^{209}Bi in the fast-neutron energy range, say, from 2 to 30 MeV; they contribute, thus, to satisfy requests and to provide means for tailoring theoretical models. Most of the data published in this energy domain are referenced in Table III for elastic scattering and Table IV for inelastic scattering, for each isotope and each incident-neutron energy, and are presented in Figs. 2–8 together with data of the present work. In these figures are also displayed as full and dashed curves the results of theoretical calculations that will be described and discussed in Sec. VII. Let us examine the data.

Concerning ^{206}Pb, elastic-scattering cross sections have been reported in eight publications, and measurements were performed at 7.00, 8.00, 8.05, 11.01, 13.70, and 21.6 MeV. The data are displayed in Fig. 2, where we notice a rather good compatibility between older data and ours. However, our differential cross sections present smaller uncertainties and span a larger angular range. For inelastic scattering on the first 3^- and 2^+ states, existing data are scarce; only two sets of measurements, at 8.0 and 4.6 MeV [45], are available in the energy range of our work (see Table IV and Fig. 5). Thus, the present work brings a significant contribution to inelastic scattering from ^{206}Pb. Looking at Fig. 5, one observes that the data of Ref. [45] for the 3^- (2.647 MeV) level are obviously larger than the calculations. Likewise, their data for the 2_1^+ (0.803 MeV) level exhibit the same behavior. Could this systematic discrepancy be caused by use of a wrong factor of normalization? As for our work, the data for the 3_1^- level show a good overall agreement with the calculated curves mentioned above; however, our forward-angle cross sections at 11.5 and 13.5 MeV look somewhat higher than the calculations and our data for the 2_1^+ level, at the same energies, though quoted with large uncertainties, seem to be in rather good agreement with calculated lines at backward angles, whereas they lie more and more above them at forward angles. How to overcome this glaring forward-angle discrepancy? On the one hand, referring to the experimental procedure, it can be argued that, for the 2_1^+ (0.803 MeV) level, neutron yields may have been overestimated at small angles because of a likely contamination by the energetically very close elastic peak. But, knowing that the effective energy resolution of our TOF spectrometer, 300 keV FWMH at 11.5 and 13.5 MeV, was sufficient to resolve two peaks separated by 800 keV, and having used a performing peak-fitting procedure (described above) to determine the yields in the peaks, we are confident that the measurements are correct. This forward-angle anomaly already mentioned above for inelastic scattering at 11.5 and 13.5 MeV on the 3_1^- level of ^{206}Pb (Fig. 5), is also observed, at the same energies, for the $(5/2^+, 7/2^+)$ doublet

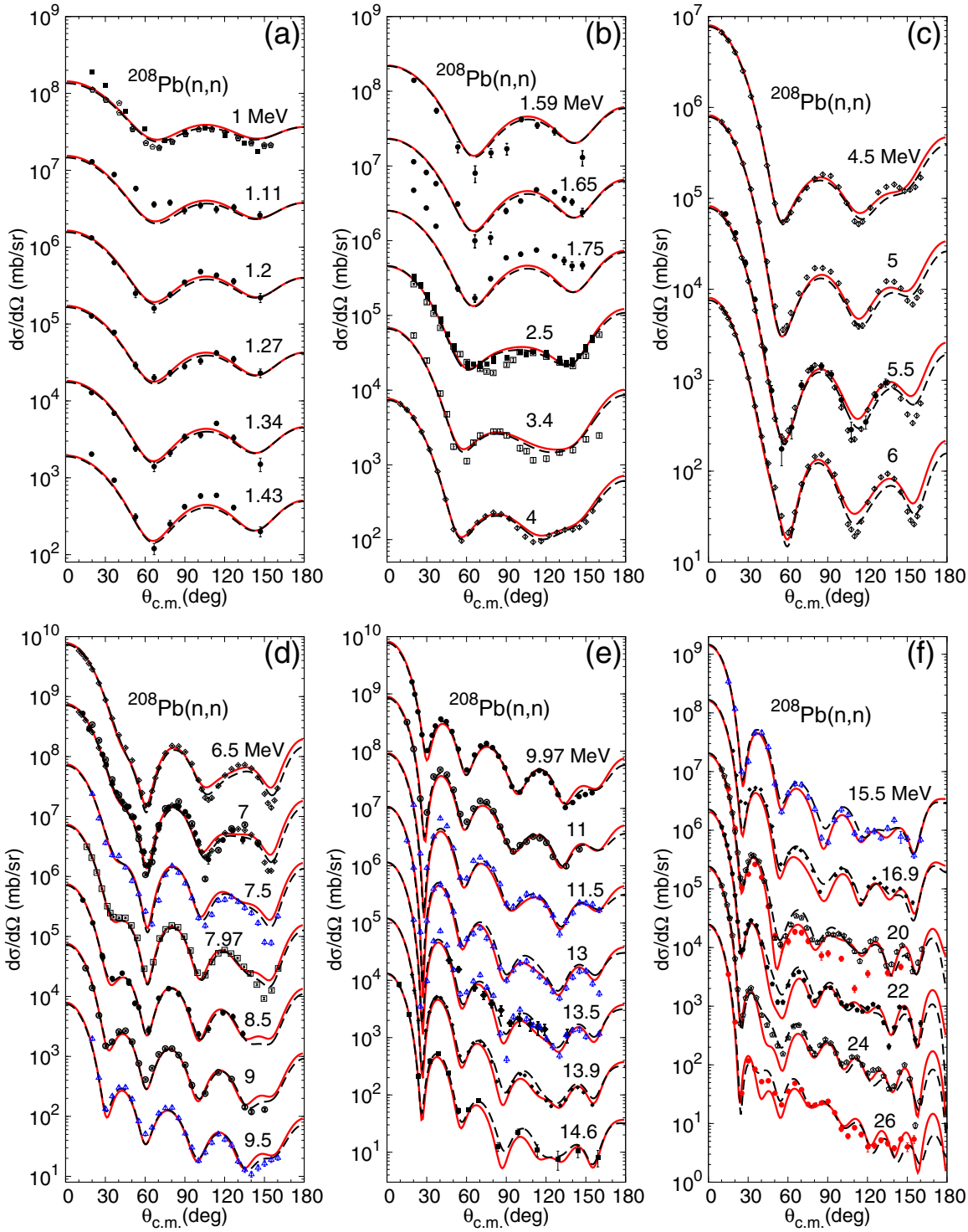

FIG. 3. Same as Fig. 2 for the ^{208}Pb(n, n) reaction. In panel (f), the data of Rapaport *et al.* [59] at 20 and 26 MeV are drawn as full red symbols in order to distinguish them from other data sets at close energies.

of ^{207}Pb and, to a certain extent, for the 2_1^+ level of ^{208}Pb (see below respectively Figs. 6 and 7); yet, the excitation energy of these levels exceeds 2.5 MeV, which precludes any contamination. In addition, this kind of anomaly has already been reported in a number of studies on inelastic scattering of fast neutrons from several nuclei [7,38,45,64]. On another hand, dealing with the theoretical analyses, it can be argued that, up to now, the various models used to interpret measurements fail to reproduce the sharp rise in the forward-angle cross-section measurements of certain excited levels in nuclei. Would it not be possible to add adequate ingredients to the models to correctly estimate the small-angle cross sections? The two

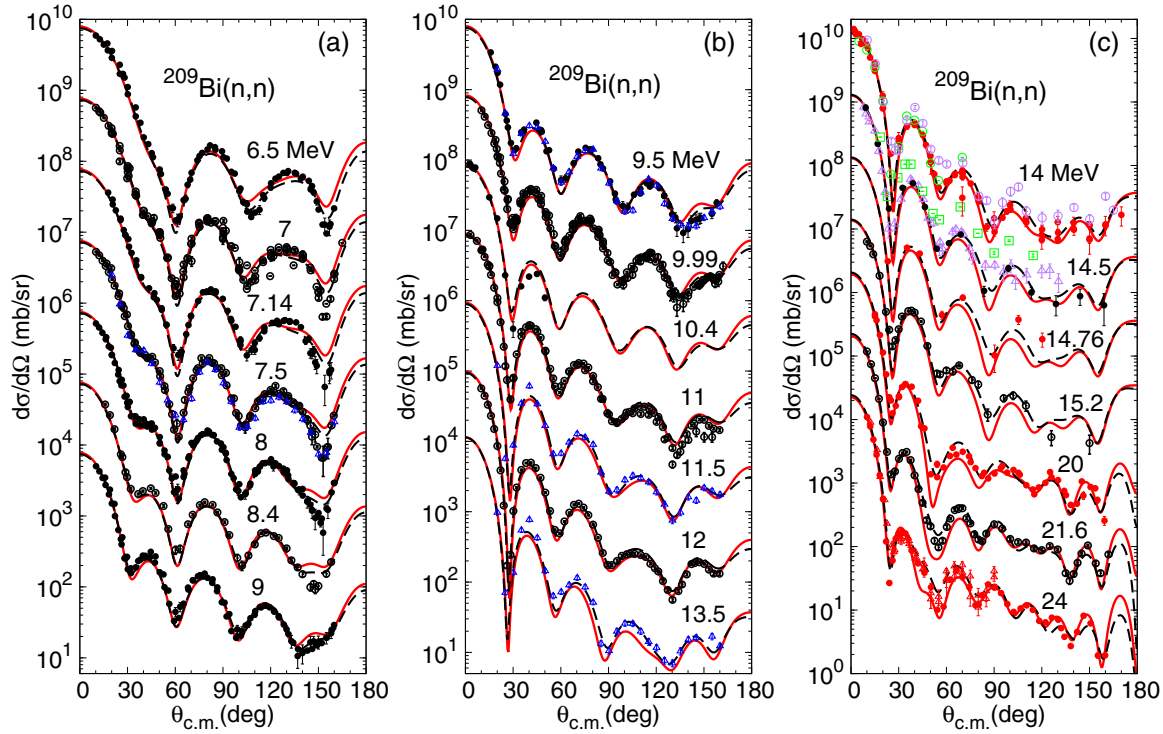

FIG. 4. Same as Fig. 2 for the ^{209}Bi(n, n) reaction. In panel (c), data sets at different energies are alternatively drawn as black and red symbols. Open green circles represent the data set of Elliot *et al.* [74] at 14.0 MeV, open purple circles represent the data set of Rayburn *et al.* [75] at 14.0 MeV, open green squares represent the data set of Strizhak *et al.* [82] at 14.5 MeV, and open purple triangles represent the data set of Cross *et al.* [83] at 14.6 MeV.

aspects of this forward-angle discrepancy will be discussed in detail in Sec. VII F 3.

To our knowledge, only two sets of measurements on ^{207}Pb have been reported for incident neutrons in the energy domain of the present work or close to it: elastic and inelastic scattering from the $(5/2^+; 7/2^+)$ doublet at 13.7 MeV [52,93] and inelastic scattering from the same doublet at energies between 5.5 and 8.5 MeV [58]. The 13.7-MeV elastic data, which span the 54–93° angular range, are plotted in Fig. 2; they look rather consistent with our data at 13.5 MeV. For inelastic scattering, the 5.5–8.5 MeV data of Ref. [58], which are displayed in Fig. 6, show a fair agreement with our measurements at 7.5 and 9.5 MeV and a fairly good agreement with calculations. However, the 13.7-MeV data are systematically higher than our 13.5-MeV data and calculations, by a factor of 2 on average. Furthermore, our forward-angle cross sections at 11.5 and 13.5 MeV are, here too, somewhat higher than our model predictions.

Concerning ^{208}Pb, measurements for elastic scattering at energies between 1.0 and 26.0 MeV have been reported in eight publications (see Table III). The various sets of data are displayed in Fig. 3 together with our measurements; this figure shows clearly a high degree of compatibility between angular distributions over the whole energy range and a fairly good agreement with the calculations; measurements performed at the same energy, or in the neighborhood, exhibit reasonable coherence. For inelastic scattering on the 3^- (2.614 MeV) level, cross-section measurements between 5.5 and 26.0 MeV have been reported in four publications. They are displayed in Figs. 7 and 8, which show, as for elastic scattering, good compatibility between the different data sets and reasonable coherence, except at 13.5 MeV, where an appreciable discrepancy between our data and those of Refs. [93] is observed. Measurements on the 5^- (3.198 MeV) level have been reported in two publications, one at energies from 5.5 to 8.0 MeV [58] and the other one at 11.0 and 25.7 MeV [95]. They are plotted in Fig. 7 which shows that our data fill in the gap between 11.0 and 25.7 MeV; it also shows some coherence between the data, but less marked since the published data are scarce in the energy range of the present work. Above this 5^- state, data have been obtained by Kinney and Perey [58] for the isolated 4^- (3.475 MeV) level at energies of 5.5 and 7.0 MeV, and, at higher excitation energies, for energy bands at 5.5, 7.0, and 8.5 MeV. For the 2^+ (4.076 MeV) level, it seems that our present data, displayed in Fig. 7, constitute the first information on this isolated state pretty well separated from the unresolved $(4^+; 6^+)$ levels centered around 4.380 MeV, the data of which are shown in Fig. 8.

For ^{209}Bi, at least 30 publications have reported elastic-scattering measurements for this isotope, in the energy range from 5.0 to 24.0 MeV (see Table III); at least 55 angular distributions were presented. The data are displayed in Fig. 4, to which have been added the four angular distributions presented here. This figure shows, here too, good compatibility between data sets at the different neutron energies, and reasonable coherence, except around 14 MeV, where large discrepancies in the differential cross sections are observed, mainly at backward angles. A thorough review of the

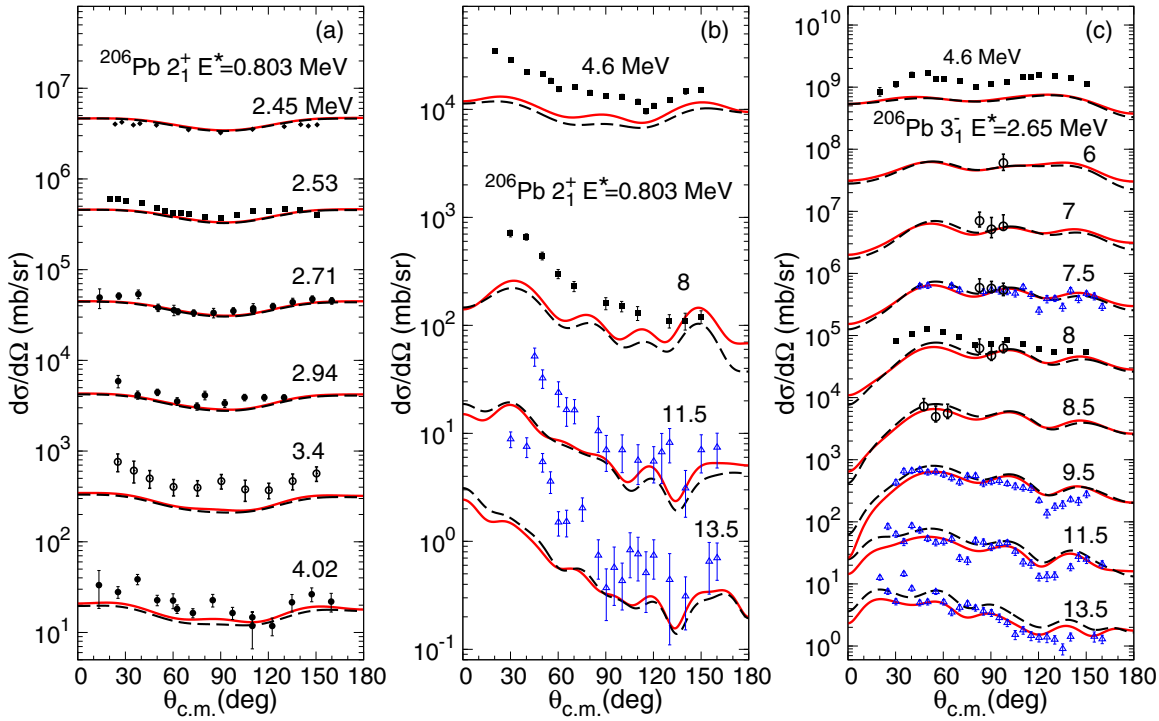

FIG. 5. Differential cross sections for neutron inelastic scattering off ^{206}Pb to the yrast 2^+ [panels (a) and (b)] and 3^- states [panel (c)]. Incident energies are indicated above each curve. Cross sections are offset by factors of 10. Data from the experiment detailed in Sec. II are represented as open blue triangles. The various other symbols represent experimental values (see Table IV). JLM-B calculations with HFB/QRPA matter/transition densities are plotted as red full curves, and calculations performed within the collective model (see Sec. VII E) are plotted as dashed black curves.

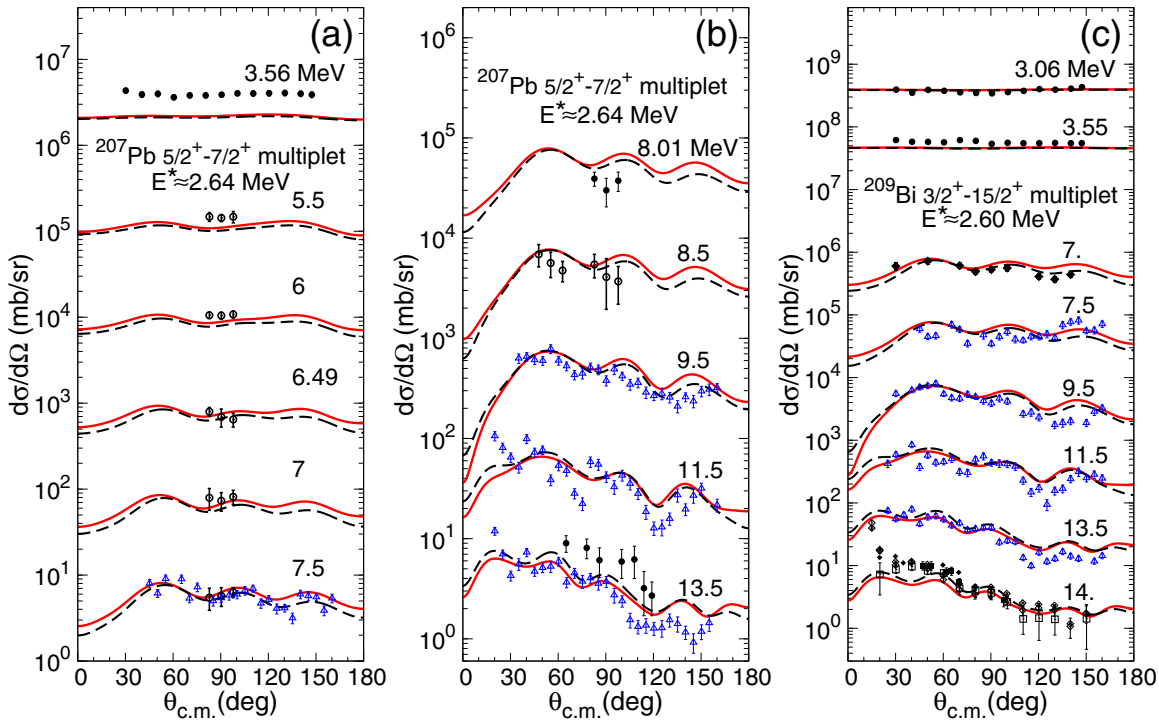

FIG. 6. Same as Fig. 5 for the ^{207}Pb [panels (a) and (b)] and ^{209}Bi [panel (c)] targets and the excitation of the $(5/2^+$-$7/2^+)$ and $(3/2^+$-$15/2^+)$ multiplets, respectively.

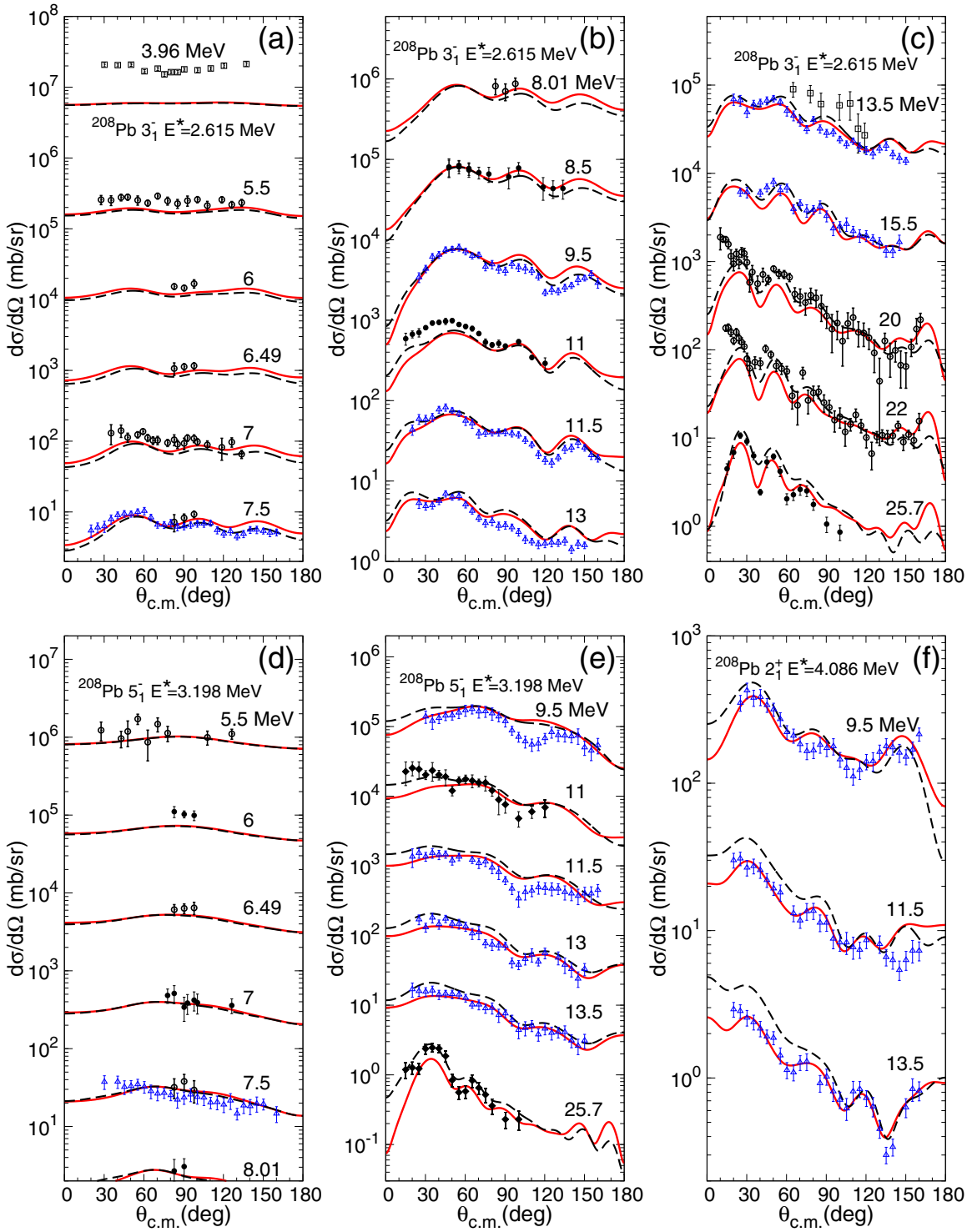

FIG. 7. Same as Fig. 5 for the ^{208}Pb target and the excitation of the 3_1^- [panels (a)–(c)], 5_1^- [panels (d) and (e)], and 2_1^+ [panel (f)] levels.

experimental studies between 14.0 and 14.5 MeV should be undertaken in order to estimate the quality of the different measurement procedures and to probably discard some works. For inelastic scattering on the ($3/2^+$, $5/2^+$, $7/2^+$, $9/2^+$, $11/2^+$, $13/2^+$, $15/2^+$) multiplet centered around 2.600 MeV, the situation is quite different. Very few data from the literature are available in the 7- to 15.5-MeV range: One measurement has been performed at 7.0 MeV [95] and five around 14 MeV [66,73,78,79,84,97]; data are plotted in Fig. 6. In between these two energies are our present measurements which fill in the gap. One can also observe in the figure an excellent agreement between measurements and calculations.

To conclude this section, it appears that the results obtained in our laboratory and presented in this paper contribute

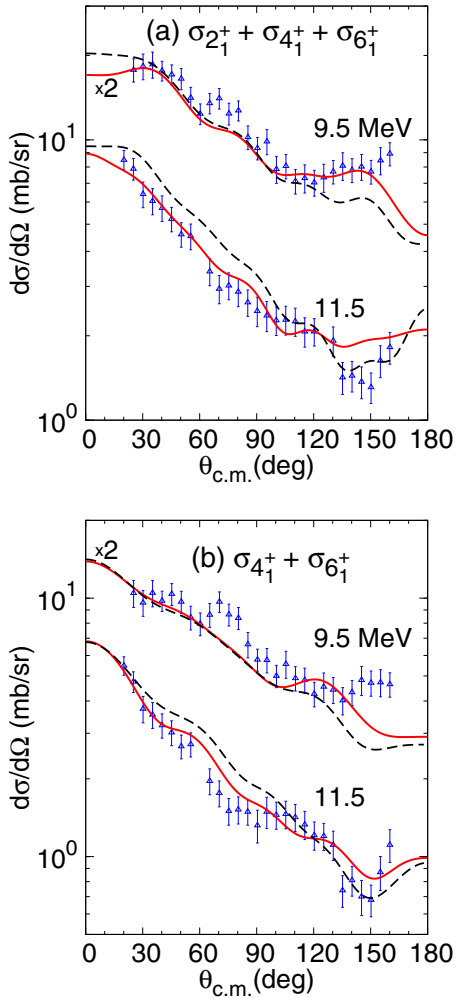

FIG. 8. Same as Fig. 5 for ^{208}Pb and for the sum of inelastic cross sections indicated on the top right corner of each plot.

markedly to complete our knowledge on fast-neutron scattering from nuclei in the region of the doubly magic shell $A = 208$.

III. JLM FOLDING MODEL

The optical and transition potentials relevant to describe the reactions of interest in this work can be calculated within the JLM folding model [6]. This theoretical microscopic approach will be referred to as model A in the next sections. It is based on a Brueckner-Hartree-Fock (BHF) calculation of the mass operator in uniform nuclear matter (NM) with Reid's hard-core nucleon-nucleon interaction, treating explicitly the Coulomb interaction and the proton-neutron asymmetry [98,99]. A local optical model potential for nucleon scattering in NM was obtained by Jeukenne *et al.* via an on-shell approximation of this mass operator [98]. An *ad hoc* procedure, the JLM folding model, allowed us to infer a complex density- and energy-dependent finite-range two-body effective interaction that is folded with local matter densities [99] to determine the potentials relevant to direct elastic and inelastic scattering processes. As nonlocality effects are approximately accounted for at the BHF level, exchange components are not to be treated explicitly in the JLM folding model.

Note that the underlying BHF calculations of the JLM interaction imply the low-density expansion where only diagrams with one hole lines are accounted for [99]. The authors commented that higher order terms are not negligible and estimated the accuracy of the first-order approximation to 20%, basing their estimate on calculations they performed at second and third orders [98]. For this reason, the authors introduced small energy-dependent normalization factors in order to better reproduce a specific set of measurements [6].

TABLE III. $\sigma(\theta)$ database for neutron elastic scattering.

Target	Energy (MeV)
^{206}Pb	3.04 [43], 3.11 [43], 3.19 [43], 3.47 [43], 3.97 [43], 4.2 [44], 4.6 [45], 5.0 [46], 7.0 [47–49], 8.0 [45], 8.05 [50], 11.01 [51], 13.7 [52], 21.6 [53]
^{207}Pb	13.7 [52]
^{208}Pb	1.0 [54,55], 1.11 [56], 1.2 [56], 1.27 [56], 1.34 [56], 1.43 [56], 1.59 [56], 1.65 [56], 1.75 [56], 2.5 [54], 3.4 [32], 4.0 [57], 4.5 [57], 5.0 [57], 5.5 [57,58], 6.0 [57], 6.5 [57], 7.0 [57–59], 7.97 [60], 8.5 [58], 9.0 [59], 9.97 [61], 11.0 [59], 13.7 [52], 13.9 [62], 14.6 [63], 16.9 [62], 20.0 [59,64], 22.0 [64], 24.0 [64], 26.0 [59]
^{209}Bi	6.5 [57,65], 7.0 [48,49,57,66–68], 7.05 [69], 7.14 [65], 7.5 [65,70], 8.0 [70], 8.03 [65] 8.05 [69], 8.09 [68], 8.4 [65], 9.0 [70], 9.06 [65], 9.5 [65], 9.99 [65], 10.0 [70], 10.4 [71], 11.0 [70,72], 11.01 [51], 12.0 [70], 14.0 [72–77], 14.1 [78–80], 14.2 [81], 14.5 [82], 14.6 [63,83],14.76 [84], 15.2 [85], 20.0 [70,86], 21.6 [53], 24.0 [70,87]

A. JLM-B effective interaction

In the present work, we use the Lane-consistent JLM-Bruyères (JLM-B) parametrization of the JLM interaction [37], which uses energy-dependent normalization for the real and imaginary parts of the potentials. These parameters were fitted to describe nucleon elastic and quasielastic scattering observables in the incident energy range 1 keV–200 MeV for spherical and near-spherical targets with mass $A = 40$ to 209 when folded with Hartree-Fock or Hartree-Fock-Bogoliubov matter densities calculated using the Gogny D1S interaction [100]. In the following, we review the main expression of the JLM-B folding model.

TABLE IV. $\sigma(\theta)$ database for neutron inelastic scattering.

Target	E^* (MeV)	J^Π	Energy (MeV)
^{206}Pb	0.803	2^+	2.2 [88], 2.24 [89], 2.45 [34], 2.5 [90], 2.53 [45], 2.71 [89], 2.94 [89,91], 3.4 [92], 4.02 [89], 4.6 [45], 8.0 [45]
	2.648	3^-	4.6 [45], 6.0 [58], 7.0 [58], 7.5 [58], 8.0 [45,58], 8.5 [58]
^{207}Pb	2.624,2.662	$(\frac{5}{2}^+, \frac{7}{2}^+)$	5.5 [58], 6.0 [58], 6.49 [58], 7.0 [58], 7.5 [58], 8.01 [58], 8.5 [58], 13.7 [93]
^{208}Pb	2.615	3^-	3.96 [94], 5.5 [58], 6.0 [58], 6.49 [58], 7.0 [58], 7.5 [58], 8.01 [58], 8.5 [58], 11.0 [95], 13.7 [93], 20. [64], 22.0 [64], 25.7 [95]
	3.198	5^-	5.5 [58], 6.0 [58], 6.49 [58], 7.0 [58], 7.5 [58], 8.01 [58], 11.0 [95], 25.7 [95]
^{209}Bi	2.493-2.741	$(\frac{3}{2}^- - \frac{15}{2}^+)$	3.06 [96], 3.55 [96], 7.0 [66], 14.0 [73,97], 14.1 [78,79], 14.76 [84]

In NM of total density $\rho = \rho_n + \rho_p$ and asymmetry $\alpha = \frac{\rho_n - \rho_p}{\rho}$, where $\rho_{n(p)}$ is the neutron (proton) NM density, the central optical potential for the elastic scattering of a nucleon with an incident energy E reads

$$\begin{aligned} &V_{\frac{n}{p}}(\rho, \alpha, E) \\ &\quad = \lambda_V(E)[V_0(\rho, E) \pm \alpha\lambda_{V_1}(E)V_1(\rho, E)] \\ &\qquad + i\lambda_W(E)[W_0(\rho, E) \pm \alpha\lambda_{W_1}(E)W_1(\rho, E)]. \end{aligned} \quad (1)$$

The index $n(p)$ indicates that the potential is for neutron (proton) scattering. The parametric form of the isoscalar (IS) $V_0(\rho, E)$ and $W_0(\rho, E)$ and the isovector (IV) $V_1(\rho, E)$ and $W_1(\rho, E)$ components are provided in Ref. [6] for the energy range 10–160 MeV and in Ref. [101] for energies below 10 MeV.

A two-body effective interaction is inferred from the optical potential in NM using the prescription

$$\mathcal{V}_{\frac{n}{p}}(|\mathbf{r} - \mathbf{r}'|, E, \rho, \alpha) = \frac{V_{\frac{n}{p}}(E, \rho, \alpha)}{\rho} g_t(|\mathbf{r} - \mathbf{r}'|), \quad (2)$$

which was first introduced by Jeukenne *et al.* [6]. The vector $\mathbf{r}$ is the projectile coordinate and $\mathbf{r}'$ is the struck target nucleon coordinate. The *ad hoc* form factor $g_t(|\mathbf{r} - \mathbf{r}'|) = (t\sqrt{\pi})^{-3} e^{\frac{|\mathbf{r}-\mathbf{r}'|^2}{t^2}}$ simulates a Gaussian range. Different ranges t are used for the real and the imaginary parts of the effective interaction. Values of the energy-dependent parameters $\lambda_V, \lambda_{V_1}, \lambda_W, \lambda_{W_1}$ and for the ranges t_V, t_W are provided in Refs. [37,102]. The prescription used to describe the spin-orbit interaction is provided in Refs. [8,37].

B. Elastic scattering

Within the JLM-B folding model, the optical potential at vector point $\mathbf{r}$ for an incident energy E is defined as

$$U_{\frac{n}{p}}(\mathbf{r}, E) = \int \mathcal{V}_{\frac{n}{p}}(|\mathbf{r} - \mathbf{r}'|, E, \rho^{(0)}, \alpha^{(0)})\rho^{(0)}(\mathbf{r}')d\mathbf{r}'. \quad (3)$$

The target local radial ground-state matter density $\rho^{(0)}(\mathbf{r})$ and asymmetry $\alpha^{(0)}(\mathbf{r})$ read

$$\begin{aligned} \rho^{(0)}(\mathbf{r}) &= \langle 0| \sum_{\sigma,\tau} \Psi^\dagger(\mathbf{r}, \sigma, \tau)\Psi(\mathbf{r}, \sigma, \tau)|0\rangle, \\ \alpha^{(0)}(\mathbf{r}) &= \frac{\rho_1^{(0)}(\mathbf{r})}{\rho^{(0)}(\mathbf{r})}, \\ \rho_1^{(0)}(\mathbf{r}) &= \langle 0| \sum_{\sigma,\tau} \tau\Psi^\dagger(\mathbf{r}, \sigma, \tau)\Psi(\mathbf{r}, \sigma, \tau)|0\rangle, \end{aligned} \quad (4)$$

where $\Psi^\dagger/\Psi(\mathbf{r}, \sigma, \tau)$ is the field creation-annihilation operator of a nucleon of spin σ and isospin τ projections at the position $\mathbf{r}$, and $|0\rangle$ represents the ground state in Dirac notation. The isospin convention is $\tau = +1(-1)$ for neutron (proton). The folding model implies a prescription for the local density approximation (LDA), namely to choose at which position we evaluate the density $\rho^{(0)}$ and the asymmetry $\alpha^{(0)}$) that define the strength of the interaction $\mathcal{V}_{\frac{n}{p}}(|\mathbf{r} - \mathbf{r}'|, E, \rho^{(0)}, \alpha^{(0)})$ between the projectile located at $\mathbf{r}$ and one of the target nucleons located at $\mathbf{r}'$. Three conventional prescriptions are to evaluate the density and the asymmetry at the projectile coordinate $\mathbf{r}$, at the target nucleon coordinate $\mathbf{r}'$, or at the midpoint $\frac{\mathbf{r}+\mathbf{r}'}{2}$. Other prescriptions are to define the potential at the arithmetic or geometric mean densities (and asymmetries), namely $\frac{\rho(\mathbf{r})+\rho(\mathbf{r}')}{2}$ or $\sqrt{\rho(\mathbf{r})\rho(\mathbf{r}')}$. Alternating between those prescriptions induces small yet non-negligible variation of the calculated observables [8]. To be consistent with the prescription which was used to establish the JLM-B parametrization, reported in Ref. [37] and selected for the present work, we rely on the LDA prescription $\rho = \rho(\mathbf{r}')$ and $\alpha = \alpha(\mathbf{r}')$; namely, we evaluate the interaction with the density and the asymmetry calculated at the target nucleon position $\mathbf{r}'$. Note that this prescription is also applied to the determination of transition potentials [see the next section, Eqs. (7)–(12)].

C. Inelastic scattering

This section is dedicated to the determination of the transition potentials to be used within the DWBA formalism.

Recasting the JLM-B effective interaction, Eq. (2), as

$$\begin{aligned} &\mathcal{V}_{\frac{n}{p}}(|\mathbf{r} - \mathbf{r}'|, E, \rho, \alpha) \\ &\quad = \mathcal{V}_0(|\mathbf{r} - \mathbf{r}'|, E, \rho) \pm \alpha\mathcal{V}_1(|\mathbf{r} - \mathbf{r}'|, E, \rho), \end{aligned} \quad (5)$$

where we have introduced the IS-IV components $\mathcal{V}_{0/1}$ defined as

$$\mathcal{V}_0 = \lambda_V V_0 + i\lambda_W W_0, \quad \mathcal{V}_1 = \lambda_V \lambda_{V_1} V_1 + i\lambda_W \lambda_{W_1} W_1, \tag{6}$$

the transition potential is written as

$$U_{\substack{n\\p}}^{0,N}(\mathbf{r}, E) = \int \mathcal{V}_0(|\mathbf{r}-\mathbf{r}'|, E, \rho^{(0)})\rho^{0,N}(\mathbf{r}') \pm \mathcal{V}_1(|\mathbf{r}-\mathbf{r}'|, E, \rho^{(0)})\rho_1^{0,N}(\mathbf{r}')d\mathbf{r}', \tag{7}$$

where $\rho_0^{0,N}$ and $\rho_0^{0,N}$ are respectively the isoscalar and isovector transition densities, defined as

$$\rho^{(0,N)}(\mathbf{r}) = \langle N| \sum_{\sigma,\tau} \Psi^\dagger(\mathbf{r},\sigma,\tau)\Psi(\mathbf{r},\sigma,\tau)|0\rangle \tag{8}$$

and

$$\rho_1^{(0,N)}(\mathbf{r}) = \langle N| \sum_{\sigma,\tau} \tau\Psi^\dagger(\mathbf{r},\sigma,\tau)\Psi(\mathbf{r},\sigma,\tau)|0\rangle. \tag{9}$$

Note that, to our knowledge, the JLM folding model was first applied to study nucleon inelastic scattering by Lagrange and Brient [12] for a ^{208}Pb target. In this early work, the transition potential was identified to the one-body potential defined in Eq. (3) where the folded isoscalar ground-state density is replaced by the isoscalar transition density between the target ground state and one target excitation, thus ignoring variations of the isovector density.

D. Rearrangement

The phenomenological description of direct elastic scattering often starts from the definition of a local optical potential $U_0(r)$ with radial shapes usually taken as a Wood-Saxon form factor $f(r;R,a) = \frac{1}{1+e^{\frac{r-R}{a}}}$ and its derivatives. In the collective model for direct inelastic scattering to vibrationnal states [1], the radius R is allowed to vibrate following the oscillations of the matter density. To first order, for a mode of angular momentum L, the transition potential reads $U_{\rm tr}(r) = \beta_L \frac{dU_0(r;R)}{dR}$, where β_L is the deformation parameter determining the strength of the transition.

Cheon [22,23] showed that the transition potential defined by Eq. (7), when using density dependent effective interactions, has to be corrected considering a rearrangement term, sometimes labeled as dynamical correction. This correction stems from the effective interaction variation with the density as the transition occurs. In the context of the JLM-B folding model, the transition potentials that include rearrangement were detailed in Ref. [17]. We only mention here the main ideas of the demonstration and the final results. We start from the ansatz that the transition potential is given by the derivation of the optical potential with respect to the isoscalar and isovector matter densities, namely

$$U_{\rm tr} = \delta\rho^{(0)} \frac{\partial U_{\rm opt}\left(\rho^{(0)}, \rho_1^{(0)}\right)}{\partial \rho^{(0)}} + \delta\rho_1^{(0)} \frac{\partial U_{\rm opt}\left(\rho^{(0)}, \rho_1^{(0)}\right)}{\partial \rho_1^{(0)}}. \tag{10}$$

Dependencies other than densities are not explicitly written for simplicity. The density variations $\delta\rho^{(0)}$ and $\delta\rho_1^{(0)}$ are identified to the IS and IV transition densities $\rho^{(0,N)}$ and $\rho_1^{(0,N)}$, defined in Eqs. (8) and (9), respectively. The transition potential can then be recast as

$$U_{\rm tr} = U_{\rm tr}^{(0)} + U_{\rm tr}^{(R)}, \tag{11}$$

where $U_{\rm tr}^{(0)} = \rho^{(0,N)}\mathcal{V}_0(\rho^{(0)}) + \tau\rho_1^{(0,N)}\mathcal{V}_1(\rho^{(0)})$ corresponds to the potential defined by Eq. (7) and $U_{\rm tr}^{(R)}$ defines the rearrangement correction that reads

$$\begin{aligned} U_{\rm tr}^{(R)} &= U_{\rm tr}^{(R_0)} + U_{\rm tr}^{(R_1)} \text{ with} \\ U_{\rm tr}^{(R_0)} &= \rho^{(0,N)}\rho^{(0)} \frac{\partial \mathcal{V}_0(\rho^{(0)})}{\partial \rho^{(0)}}, \\ U_{\rm tr}^{(R_1)} &= \rho^{(0,N)}\tau\rho_1^{(0)} \frac{\partial \mathcal{V}_1(\rho^{(0)})}{\partial \rho^{(0)}}. \end{aligned} \tag{12}$$

These expressions are strictly equivalent to those of Cheon *et al.* (see Eq. (47) in Ref. [23]).

We will illustrate in Sec. VII D how this rearrangement correction impacts nucleon direct inelastic cross sections magnitude.

IV. (Q)RPA DESCRIPTION OF THE NUCLEAR STRUCTURE

The nuclear structure ingredients required in the modeling of elastic and inelastic nucleon scattering are the proton, neutron, and charge ground state, and the transition densities between the ground state and the various levels studied in Sec. VII. Transition densities in even-even nuclei are obtained from (Q)RPA calculations performed with the Gogny D1S interaction [100], built from a HF(B) calculation with the same interaction. Details on the QRPA method implemented with Gogny D1-type functionals are provided in Refs. [27,28,103] and references therein (see Refs. [104,105] for the RPA method). Nuclear structure properties are accurately predicted by this (Q)RPA model, for low-energy collective states as well as giant resonances, for both spherical [27,103–105] and axially deformed nuclei [28,103]. We review here the main features of the QRPA approach for spherical nuclei. The RPA is applicable to the doubly closed-shell nuclei for which pairing correlations vanish. An excitation of the target is modeled by a phonon excitation on a correlated ground state $\tilde{0}$, namely

$$|N\rangle = \Theta_N^\dagger \sum_{ij} \left(X_{ij}^N \eta_i^\dagger \eta_j^\dagger - Y_{ij}^N \eta_i \eta_j\right), \quad \text{with } \Theta_N^\dagger|\tilde{0}\rangle = 0 \ \forall N. \tag{13}$$

The quantum number N stands for $N \equiv kJ\Pi M$, where J is the total angular momentum, M is its projection on the symmetry axis, Π is the parity of the excitation, and k distinguishes between various states with the same $J\Pi M$ quantum numbers. Our study is restricted to transitions between the ground state and natural parity excitations, i.e., with parity $\Pi = (-)^J$. The operator $\eta_i^\dagger$ (η_i) is the creation (destruction) quasiparticle operator. The HFB and QRPA codes are implemented in a cylindrical harmonic oscillator basis. Calculations were performed in a basis including 15 major shells to ensure converged values of nuclear structure properties.

As depicted in Sec. III, three different nuclear structure properties of interest for our reaction studies are the excitation energies, reduced transition probabilities, and local radial matter and transition densities. The proton, neutron, and charge matter densities are folded with the JLM-B interaction to provide the optical potential for neutron and proton scattering. Several works along this line with HF(B) densities with the D1S interaction are reported in the literature (see, for instance, Ref. [8]); thus, we will focus here on the nuclear structure ingredients for inelastic scattering. We will next compare the nuclear structure properties predicted by the (Q)RPA model to available experimental values for the excitations studied in Sec. VII E, for the targets ^{206,208}Pb. The case of the two odd-nuclei ^{207}Pb and ^{209}Bi will be discussed later.

A. Transition between ground and one phonon states for ^{206,208}Pb

The local point-neutron and -proton transition densities for a transition from the correlated (Q)RPA ground state $|\tilde{0}\rangle$ to an excitation $|kJ\Pi M\rangle$ read

$$\rho^{(n,p)}_{kJ\Pi M}(\mathbf{r}) = \langle kJ\Pi M| \sum_{i=1}^{(N,Z)} \frac{\delta(r-r_i)}{r_i^2} Y^L_M(\Omega_i)|\tilde{0}\rangle$$
$$= \rho_{kJ\Pi}(r) Y^L_M(\Omega)\delta_{JL}, \quad (14)$$

where $N(Z)$ is the number of neutrons (protons) of the considered nucleus. As we deal with even-even nuclei, we always have $L = J$. The charge ground state or transition density $\rho^{(c)}(r)$ is determined by smearing the corresponding proton and neutron point densities, considering the proton and neutron finite charge distributions, as well as a correction from the center-of-mass motion [106].

The proton and neutron reduced matrix elements are defined as

$$M^{(L)}_{p/n} = \int r^{2+L} \rho^{(p/n)}_{N,L}(r) dr. \quad (15)$$

The reduced charge transition probability $B(EL\uparrow)$, for an electric transition from the ground state to an excited state, reads

$$B(EL\uparrow) = e^2(2L+1)\left| \int r^{2+L} \rho^{(c)}_{N,L}(r) dr \right|^2, \quad (16)$$

where e is the elementary electric charge. We note that the calculation of this quantity is performed with the charge transition density. The same calculation performed with point-proton transition density leads to variations smaller than 0.1%.

We introduce the neutron-to-proton reduced matrix element ratio

$$R_{np} = \frac{\tilde{M}_n}{\tilde{M}_p} = \frac{Z}{N}\frac{M_n}{M_p}, \quad (17)$$

where we have removed the mention to multipole L to keep our notations light.

We display in Tables V and VI reduced transition probabilities and excitation energies for levels in ^{208,206}Pb. The (Q)RPA/D1S structure model overpredicts the low-lying state excitation energies by 500 keV to 1.5 MeV. For instance, yrast octupole excitation in ^{208,206}Pb, located at roughly 2.6 MeV, are predicted at 3.1 MeV by the present (Q)RPA approach. This discrepancy could be related to the couplings to two particle-hole configurations (four quasiparticles) that are not included in the (Q)RPA phonon operator. Such an effect was recently accounted for within the double RPA method [107], which shows a downward shift of low-lying excitations in ^{16}O. Such a method, if applicable in the $A = 208$ mass region, would probably shift downward the predicted excitation energies, thus getting closer to experimental energies. We note that calculations employing the D1M parametrisation [108] (not displayed here) do not reduce the discrepancy between (Q)RPA and experimental excitation energies. Calculations with a different functional form for the effective interaction, such as the D2 interaction [109], may eventually reduce this discrepancy. We note that the impact of this shift in energy on calculated direct inelastic cross sections studied in the present paper is very small for incident energies well above the level threshold (see discussion at the end of Sec. III).

TABLE V. Reduced transition probabilities and excitation energies in ^{208}Pb. Adopted values [116] are compared to RPA predictions.

	$B^{\rm exp}(EL\uparrow)$	$B^{\rm RPA}(EL\uparrow)$	$E_{\rm exp}$	$E_{\rm RPA}$
J^Π_k	$[10^{2L}\ {\rm e}^2\ {\rm fm}^{2L}]$		[MeV]	
3^-_1	0.611(12)	0.692	2.614	3.421
5^-_1	0.0447(30)	0.0553	3.197	4.407
2^+_1	0.318(13)	0.296	4.085	4.603
4^+_1	0.155(11)	0.149	4.323	5.507
6^+_1	0.067(7)	0.0327	4.422	5.816

Excitation energies, ground state, and transition matter densities as well as reduced transition probabilities for ^{208}Pb have been analyzed in Refs. [104,110,111] within the RPA model with the D1 interaction [112]. The same observables obtained with the D1S interaction are analyzed in Refs. [113–115] and display the same good agreement with measurements. As a reminder, we provide in Table V a comparison between RPA/D1S reduced transition probabilities for the five transitions that are analyzed in the nucleon inelastic scattering study of Sec. VII. All predicted reduced transition probabilities but one are in good agreement with the adopted values. One exception is for the $0^+ \to 6^+_1$ transition for which the predicted RPA value is half that of the adopted one.

TABLE VI. Same as Table V for ^{206}Pb and QRPA predictions. The sign $(*)$ indicates that no uncertainties are given.

	$B^{\rm exp}(EL\uparrow)$	$B^{\rm QRPA}(EL\uparrow)$	$E_{\rm exp}$	$E_{\rm QRPA}$
J^Π_k	$[10^{2L}\ {\rm e}^2\ {\rm fm}^{2L}]$		[MeV]	
2^+_1	0.101(3) [117]	0.099	0.803	1.505
4^+_1	0.0167(*) [117]	0.0195	1.684	2.580
7^-_1	$1.54\ 10^{-3}$(*) [118]	$1.40\ 10^{-3}$	2.200	2.749
3^-_1	0.65(4) [117]	0.635	2.648	3.732
5^-_1		0.0106	2.782	3.163
$2^+_{\rm IS\text{-}SV}$	0.23(2) [117]	0.213	4.102	5.083

TABLE VII. R_{np} [see Eq. (17)] ratios for transitions in ^{206}Pb. Values predicted from the present QRPA analysis with the Gogny D1S force (second column) are compared to those found in the literature. Values in the last column (QRPA*) are those from Table I of Ref. [119], and result from a quasiparticle RPA calculation with separable isoscalar and isovector particle-hole interactions, as described in Ref. [122]. $2^+_{\text{IS-SV}}$ is the quadrupole surface vibration mode located at 4.102 MeV.

J^Π_k	QRPA This work	RPA/(p,p') 650 MeV [118]	$(O^{17}, O^{17\prime})$ 375 MeV [119]	$(\pi^\pm, \pi^{\pm\prime})$ 180 MeV [120]	(p,p') 650 MeV [121]	QRPA* [119,122]
2^+_1	1.40	1.28	1.65	1.65(11)	1.51(5)	1.45
4^+_1	1.33	0.96			1.02	
7^-_1	1.86	1.59				
3^-_1	1.03		1.00	1.00(7)	0.99(7)	0.99
5^-_1	1.30			1.00(7)		
$2^+_{\text{IS-SV}}$	0.972	0.99	1.00	1.00(7)	1.30(9)	1.11

We now focus on QRPA prediction for ^{206}Pb. We compare in Table VI available experimental data to calculated reduced charge transitions probabilities. The calculated $B(EL)$ values lie within error bars for the yrast quadrupole and octupole excitations, as well as for the isoscalar surface vibration (IS-SV) 2^+ level located at $E_{\text{exp}} = 4.102$ MeV (labeled $2^+_{\text{IS-SV}}$ in the following). This level is of same nature as that for the yrast quadrupole excitations in ^{208}Pb located at 4.085 MeV. We remind that such IS-SV levels are characterized by a radial transition density which is peaked at the nuclear surface and displays a matrix elements ratio $\frac{M_n}{M_p} \simeq \frac{N}{Z}$. For the 7^-_1 and 4^+_1 states, the predicted strengths are respectively 10% and 17% higher than the reported experimental values, for which no error bar is provided. We display in Table VII the ratios R_{np} for these excitations. Values predicted within the present QRPA approach are mostly in good agreement with those inferred from proton, pion, and ion inelastic scattering measurements and previous (Q)RPA calculations. The only exceptions are for the 4^+_1 and 7^-_1 states for which values exceed those inferred from proton inelastic scattering measurements. A specific discussion is devoted to the 2^+_1 excitation in neutron and proton scattering in Sec. VII F 2.

A comparison between calculated (QRPA) and empirical charge transition densities is displayed in Fig. 9 for the excited states (a) 2^+_1, (b) 4^+_1, (c) 7^-_1, and (d) $2^+_{\text{IS-SV}}$ in ^{206}Pb. The calculated QRPA neutron and proton densities [Eq. (14)] that are used in the JLM-B folding model to generate nuclear transition potentials are also displayed as black dashed and dotted curves, respectively. Empirical charge densities surface peak magnitudes are well reproduced, except for the 4^+_1 state, for which the magnitude is 1.35 times the empirical one. Positions of the surface peaks are also well reproduced except for the calculated 2^+_1 transition, with a maximum located at a radius 0.25 fm larger than that of the experimental one.

In conclusion, as observed in previous analyses of the ^{208}Pb nucleus within the D1S/RPA approach [104,110,111], transition strengths for many low-energy excitations in ^{206}Pb are accurately described by the QRPA/D1S model.

B. Odd nuclei

The ground-state densities of the two odd nuclei ^{207}Pb and ^{209}Bi that we use in the present folding model are determined within the HFB method by blocking the $3p\frac{1}{2}$ neutron hole state for ^{207}Pb and the $1h\frac{11}{2}$ proton particle state for ^{209}Bi.

Excited states considered in the present analysis, namely the members of the $L = 3$ multiplet, for the even-odd ^{207}Pb and odd-even ^{209}Bi nuclei are described within the weak coupling approximation [73], which has been proven to be well suited to describe the octupole surface vibration states for those two nuclei [73,124]. For ^{207}Pb, the octupole multiplet stems from the coupling of the octupole phonon excitation in the ^{208}Pb core, which lies at 2.64 MeV, to the $3p\frac{1}{2}$ neutron single particle state to provide the $(\frac{5}{2}^+, \frac{7}{2}^+)$ multiplet, experimentally located at 2.624 and 2.662 MeV, with a centroid at 2.643 MeV. In ^{209}Bi, the first octupole multiplet $(\frac{3}{2}^+, \frac{5}{2}^+, \frac{7}{2}^+, \frac{9}{2}^+, \frac{11}{2}^+, \frac{13}{2}^+, \frac{15}{2}^+)$, lying in the excitation energy range 2.493–2.741 MeV (energy centroid at 2.617 MeV),

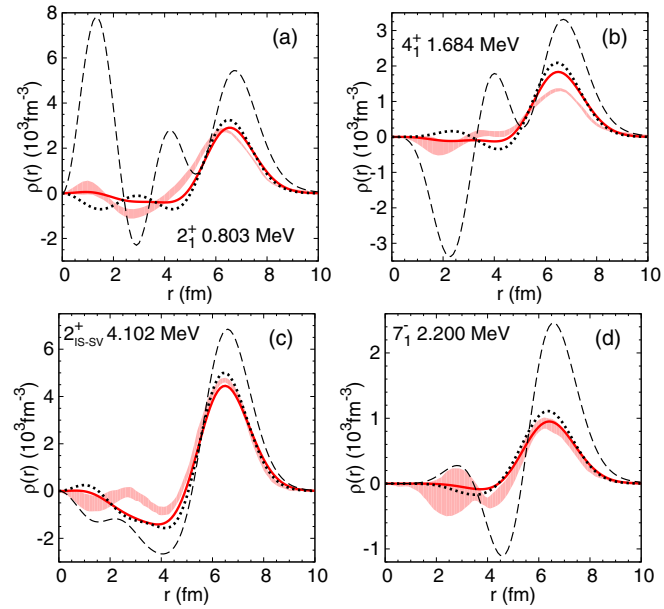

FIG. 9. Calculated radial charge transition densities for (a) 2^+_1, (b) 4^+_1, (c) 7^-_1 and $2^+_{\text{IS-SV}}$ levels (full red curves) in ^{206}Pb compared to empirical ones (shaded red areas) extracted from (e,e') experiments [118,123]. Calculated point-neutron (dash black curves) and point-proton (dotted black curves) densities are also represented.

is described by coupling the ^{208}Pb core 3_1^- phonon excitation, lying at 2.614 MeV, to the $1h\frac{11}{2}$ single-particle proton state. Within the weak-coupling approximation, the centroid of the levels' multiplet, resulting from the coupling of a nucleon to a core vibration, should coincide with the energy of the vibration in the adjacent even nuclei, which is closely verified here. Transition potentials for inelastic scattering (reaction model B) are determined from transition densities in the adjacent even core (see Sec. VI).

V. COLLECTIVE MODEL FOR DIRECT INELASTIC SCATTERING

In order to quantify the quality of the agreement between measured cross sections and calculations from the microscopic model depicted in Secs. III and IV (model A), we include in our comparisons results from a phenomenological optical model for elastic scattering, and from the collective model [1] for inelastic scattering. This theoretical phenomenological approach will be referred as to model B in the next sections. Indeed, phenomenological collective models were widely used to interpret hadron inelastic scattering data and infer nuclear structure properties from them, such as deformation parameters and neutron to proton matrix elements ratios.

We note that the collective model for hadron inelastic scattering defines the potential describing a transition between the ground state with $J_0 = 0$ (even-even target) and an excitation of spin $J = L$, as

$$U_L^{(x)}(r) = -\beta_L^{(P)} R_x \frac{dU_x(r)}{dr}, \tag{18}$$

where $U_x(r)$ is one of the local optical potential component, the superscript or subscript x stands for real or imaginary central or spin-orbit potentials, $\beta_L^{(P)}$ is the deformation parameter, and the superscript P stands for (n, n') or (p, p'). We mention that in the DWBA framework inelastic scattering cross sections exactly scale as $(\beta_L^{(P)})^2$.

Within the collective model for vibration and for an angular momentum transfer $L \geqslant 2$, a charge deformation parameter $\beta_L^{(C)}$ can be related to the reduced charge transition probability [1] by

$$\beta_L^{(C)} = \sqrt{B(EL\uparrow)}\frac{4\pi}{3ZR^L} \quad \text{with} \quad R = 1.2A^{\frac{1}{3}}. \tag{19}$$

To calculate inelastic scattering cross sections, we performed DWBA calculations using the phenomenological Koning-Delaroche (KD) optical potential to determine both the distorted waves and the transition potentials. The same deformation parameter is used for the central and spin-orbit potentials (for both real and imaginary parts). We used the prescription depicted in Sec. VII A 3 to determine the energies at which the KD potentials are determined.

The $\beta_L^{(C)}$'s (see Table VIII) were computed considering the adopted $B(EL\uparrow)$ values shown in Tables V and VI for ^{208}Pb and ^{206}Pb, respectively. The only exception is for the 5_1^- state in ^{206}Pb for which we used the QRPA $B(EL\uparrow)$ value since, to our knowledge, no experimental value is reported for this level.

TABLE VIII. Charge deformation parameters and deformation parameters used in nuclear transition potentials for the collective model studies of (n, n') and (p, p') differential cross sections. Coulomb deformations and those used for neutron scattering [considered equal as explained in Sec. V] are provided in the third column, entitled $\beta_L^{(C/nn')}$. Deformations used for the nuclear transition potential for proton scattering are provided in the fourth column, entitled $\beta_L^{(pp')}$. In this last column, the letters a, b, and c in exponents are for the proton incident energy 35, 19.64, and 24.5 MeV, respectively. See Secs. V and VI for more details.

Target	J_k^Π	$\beta_L^{(C)/(n,n')}$	$\beta_L^{(p,p')}$
^{206}Pb	2_1^+	0.03216	0.044^a 0.048^b
^{206}Pb	4_1^+	0.0262	0.0262^a 0.0320^b
^{206}Pb	7_1^-	0.0223	0.0190^a
^{206}Pb	3_1^-	0.11570	0.095^a 0.100^b
^{206}Pb	5_1^-	0.0294	0.0235^a
^{206}Pb	$2^+_{\text{IS-SV}}$	0.04717	$0.040^{a,c}$
^{208}Pb	3_1^-	0.11109	
^{208}Pb	5_1^-	0.05944	
^{208}Pb	2_1^+	0.05698	
^{208}Pb	4_1^+	0.07870	
^{208}Pb	6_1^+	0.10235	
^{207}Pb	$\frac{5}{2}^+, \frac{7}{2}^+$	0.11570	
^{209}Bi	$\frac{3}{2} - \frac{15}{2}^+$	0.11109	

For neutron inelastic scattering calculations, we assume $\beta_L^{(n,n')} = \beta_L^{(C)}$, considering that neutron scattering are essentially sensitive to proton distributions, as the neutron-proton interaction is known to be approximately three times stronger than the interaction between alike particles for energies below 50 MeV [125].

For proton inelastic scattering off ^{206}Pb, that will be discussed in Sec. VII F 3 a, as low-energy excitations are not isoscalar surface vibration and protons mainly probe neutron density, we did not assume $\beta_L^{(p,p')} \simeq \beta_L^{(C)}$. Coulomb excitation is calculated considering charge deformations $\beta_L^{(C)}$ provided in Table VIII, but the nuclear deformations $\beta^{(p,p')}$ were adjusted to approximately reproduce the various observed (p, p') magnitudes. Thus, $\beta^{(p,p')}$ is allowed to vary between different incident proton energies.

VI. DWBA CALCULATIONS FOR ODD-A NUCLEI

Here we detail the approximation followed to perform DWBA calculations from models A and B for inelastic scattering to states members of the octupole multiplet in the two odd-A nuclei ^{207}Pb and ^{209}Bi. We use the excited-core approximation which assumes that nucleon inelastic scattering by the odd-A nucleus is very similar to that by the core alone [126,127].

For model B, this approximation implies that the transition potential between the ground state (spin J_0) and one excited state belonging to the octupole multiplet (spin J with $|J_0 - L| \leqslant J \leqslant J_0 + L$) is calculated from Eq. (18) using the deformation parameter

$$\beta_{J,L}^{(P)} = \sqrt{C_{LJJ_0}}\beta_L^{(P)}, \tag{20}$$

with

$$C_{LJJ_0} = \frac{2J+1}{(2L+1)(2J_0+1)}, \tag{21}$$

where $\beta_L^{(P)}$ is the deformation parameter used for the core nucleus.

We note that direct inelastic cross sections for the odd-A nucleus are related to that of the core according to

$$\frac{d\sigma_L^{(\text{core})}}{d\Omega} = \sum_{J=|J_0-L|}^{J_0+L} C_{LJJ_0} \frac{d\sigma_{J,L}^{(\text{odd-A})}}{d\Omega} \tag{22}$$

and $\sum_{J=|J_0-L|}^{J_0+L} C_{LJJ_0} = 1$.

In the present work, for both models A and B, we describe ^{207}Pb as a neutron particle on a ^{206}Pb core, and ^{209}Bi as a proton particle state on a ^{208}Pb core. For model B, transition potentials are determined from Eq. (20) considering the $\beta_L^{(nn')}$ value for ^{206}Pb or ^{208}Pb (see Table VIII). For model A, transition potentials are calculated from the point-proton and -neutron transition densities [see Sec. IV, Eq. (14)], for the 0^+ (ground state) $\rightarrow$ 3_1^- transition in ^{206}Pb or ^{208}Pb.

VII. ANALYSIS OF THE CROSS SECTIONS

This section is dedicated to the analysis of differential elastic and inelastic scattering cross sections. New data presented in Sec. II are compared to the results of the model A, namely the JLM-B folding model applied with the HF(B)/(Q)RPA nuclear structure approach depicted in Sec. IV, and of the model B, namely the phenomenological KD optical potential and the collective model, as depicted in Sec. V. Additional specificities of the present calculations of direct elastic and inelastic cross sections are given in Sec. VII A. Section VII B provides details on the contributions of the compound process for both elastic and inelastic scatterings. Specificities of model A and B for odd-A targets are explained in Sec. VI.

For elastic scattering, and inelastic scattering to the excited states for which new data are presented in Sec. II, all existing experimental data sets for incident energy in the range 4–27 MeV are compared to our calculations. In specific cases, calculations and experimental data are also compared in the 1- to 4-MeV range in order to shed light on the coherence between various experimental data-sets. The elastic scattering data are analyzed in Sec. VII C. Prior to the inelastic scattering data analysis in Sec. VII E, we discuss in Sec. VII D how rearrangement corrections impact inelastic cross sections. A discussion motivated by the observation of clear mismatches between model calculations and measurements is provided in Sec. VII F.

A. Details on the direct cross-section calculation within the microscopic JLM-B folding model

In the following, we detail practical choices made for our calculations.

1. Consistent approach

The optical potential for elastic scattering are calculated within the JLM-B folding model as described in Sec. III B. The DWBA calculations for direct inelastic scattering are performed considering (i) incoming and outgoing distorted waves calculated with optical potentials obtained from Eq. (3) and (ii) transition potentials calculated from Eq. (12). The DWBA calculations are thus consistent, in the sense that the same reaction model, the JLM-B folding model, is used to generated both the distorted waves and the transition potentials. Additional details are provided below.

2. Ground-state densities

We use the HFB ground-state densities to determine the optical potentials, following Eq. (3) and the density-dependent interaction in the transition potentials (12). A better choice may have been to use the correlated ground-state densities calculated from the QRPA model. This approximation is justified considering the two following aspects. First, the JLM-B interaction parameters were obtained when the interaction was folded with HFB densities. Switching to QRPA densities would require a new fit if one wanted to reproduce elastic scattering observables as accurately as in Refs. [8,37]. Second, the previous study [114] showed that ground-state long-range correlations, as RPA ones, only slightly impact on elastic scattering observables at energies below approximately 100 MeV. So we expect that neglecting the (Q)RPA correlations in the ground-state densities would not strongly impact the reaction observables predicted here.

3. Potential energy dependence

The channel energy dependence was accounted for: The optical potential, Eq. (3), which is used to determined the outgoing distorted wave that enters the definition of the DWBA transition amplitude, was calculated at the center of mass energy $E = E_{in} - E_x$, where E_{in} is the center-of-mass incident energy and E_x is the target-state excitation energy. The transition potential, Eq. (7), and the rearrangement corrections, Eq. (12), were determined following the prescription which consists in calculating the effective interaction at the midenergy $E = E_{in} - \frac{E_x}{2}$. Those prescriptions were first used by Meigooni *et al.* [128] in a coupled channel framework. This study showed that neglecting this dependency could strongly impact the predicted inelastic scattering magnitude. This effect is of particular importance as we approach the inelastic threshold energy.

4. Excitation energies

In the inelastic scattering calculations, we use experimental excitation energies rather than the predicted ones. Usually the calculated QRPA excitation energy differs from the experimental values by approximately 500 keV to 1 MeV (see, for instance, Fig. 1 of Ref. [129]). For incident energies sufficiently larger than the reaction threshold energy, changing this prescription does not impact the calculated cross sections since the effective interaction varies slowly with energy. However, as we get closer to the inelastic channel threshold, we need to use the experimental excitation energies for accurate calculations, especially for determining the compound nucleus components.

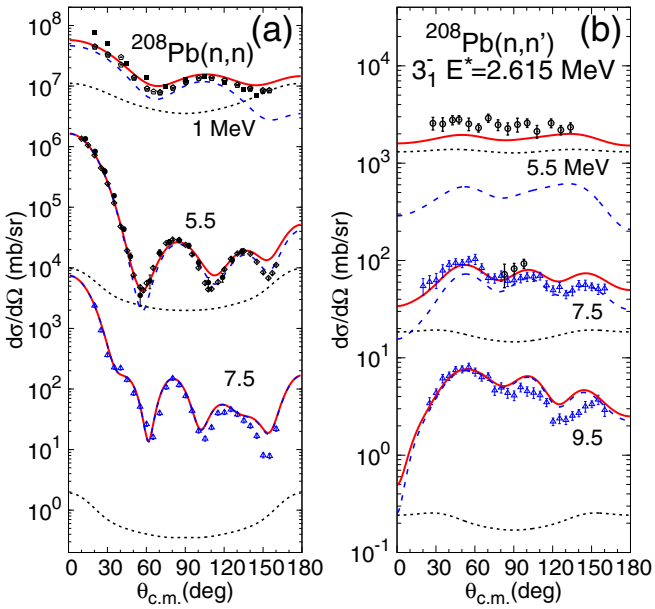

FIG. 10. Differential cross sections for (a) neutron elastic scattering and (b) inelastic scattering to the 3_1^- level (right panel) for a ^{208}Pb target. Incident energies are indicated above each curve. Cross sections are offset by factors of 200 (10) for elastic (inelastic) scattering. Symbols represent experimental data (see references in Tables III and IV). Contributions from the direct processes are plotted as dashed blue curves, and those from the compound processes as are plotted as dotted black curves. The sum of these contributions are plotted as full red curves.

All cross sections for direct elastic and inelastic scattering were calculated with the code ECIS06 [130].

B. Compound nucleus contributions

In the $A = 208$ region, for neutron scattering below 8–10 MeV, emission from compound nucleus (CN) processes is not negligible as compared to the direct emission. CN contributions, to elastic scattering cross section and to inelastic scattering cross section for each excited state we analyzed, are calculated within the Hauser-Feshbach formalism, including the Moldauer's width fluctuation corrections [131,132], with the computer code TALYS [133]. To asses the quality of our direct reaction modeling through the comparison to experimental angular distributions, we need to have a good idea of the relative contributions of direct and compound processes for the various reaction we analyzed. To provide the reader with this information, we detail in Figs. 10(a) and 10(b) these various contributions to the differential neutron elastic and inelastic cross sections for a ^{208}Pb target at three different energies. Above 1 MeV, the direct process (dashed blue curves) strongly contributes to elastic scattering, while the compound component (dotted black curves) gets very small for incident energies above 6–7 MeV [see Fig. 10(a)]. For inelastic scattering [Fig. 10(b)], the direct component is weak for incident energies below 5 MeV (given the present excitation energy of 2.614 MeV) and the compound component vanishes above 10 MeV, thus 7 MeV above the excitation threshold. These behaviors are quite similar for all reactions analyzed in the present work, though for a specific incident energy and a specific outgoing channel, the magnitude of the CN contribution could strongly varies from one target nucleus to another, according to the number of open channels between which compound emission is shared.

C. Analysis of differential elastic (n, n) data

An extensive analysis of elastic scattering data for both proton and neutron with the JLM-B folding model and HFB/D1S matter densities has been reported in Refs. [8,37] for spherical and near-spherical nuclei. We compare in Figs. 2 to 4 the new measured angular distribution presented in Sec. II to data from experiments in the 3- to 26-MeV energy range (see database with references in Table III). Calculations performed using the folding model described in Sec. III or with the phenomenological global KD potential [134] are displayed as full and dashed curves, respectively.

An overall good agreement between measurements and calculations is observed for the four targets. Beyond this general feature, we note some local discrepancies between various measurements and calculations. The most significant of them are detailed below.

For $E > 13$ MeV, the JLM-B folding model slightly underestimates the measured differential cross sections at medium scattering angles [see Fig. 2(b) for ^{206}Pb, Fig. 2(c) for ^{207}Pb, Figs. 2(e) and 2(f) for ^{208}Pb, and Figs. 4(b) and 4(c) for ^{209}Bi]. This feature is also seen for various targets in the previous analyses using JLM folding model [8,37]. Calculations with the phenomenological KD potential display a similar problem only at 11.5 and 13.5 MeV. Note that a similar discrepancy is seen in a recent folding model analysis based on relativistic BHF calculations (see Fig. 14 of Ref. [135]).

For the ^{208}Pb target at 20 MeV [see Fig. 3(f)], the data of Finlay *et al.* [86] (open black symbols) agree quite well with our calculations, while data of Rapaport *et al.* [59] (full red circles) appear to be small at angles above 80°. Similarly, for the ^{209}Bi target at energies in the 14- to 15-MeV range [see Fig. 4(c)], a good coherence is found between most of the measurements and our calculations. However, four data sets, that correspond to those of Refs. [74,75,82,83], depart from this reasonable agreement between measurements and calculations. This calls for a revision of these data sets as already mentioned in Sec. II B 2.

D. Impact of rearrangement corrections on inelastic cross sections

In this section, we illustrate the importance of considering the rearrangement component [see Eq. (12)] when analyzing inelastic scattering to discrete state reactions within the JLM-B folding model (model A).

Figure 11(a) displays the ratio of angle integrated inelastic cross section calculated with the rearrangement corrections (labeled σ_R) to that without those corrections (labeled σ_0), for the yrast excitations in ^{208}Pb with angular momentum in the range $L = 2$–8. As seen in this plot, for the incident neutron energy range of the present study, namely

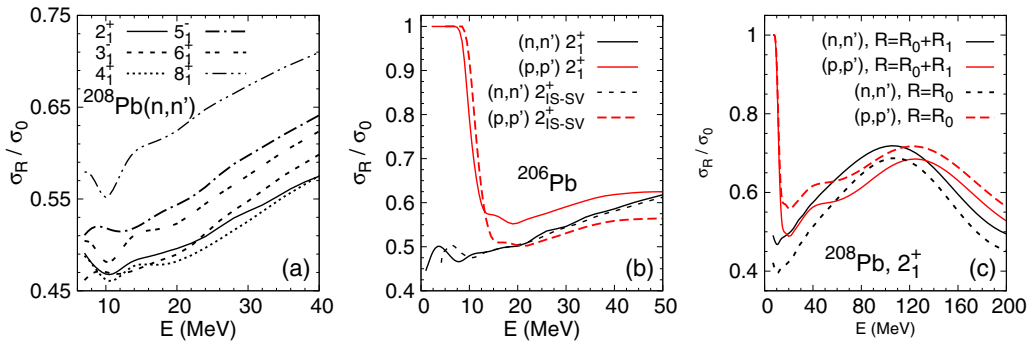

FIG. 11. (a) Ratios of the angular integrated inelastic cross sections calculated with rearrangement (σ_R) to that without those corrections (σ_0) as a function of neutron incident energy in the case of neutron inelastic scattering for the various levels indicated in the plot. (b) Same ratios for both neutron (black curves) and proton (red curves) inelastic scattering to the 2^+_1 (full curves) and $2^+_{\text{IS-SV}}$ (dashed curves) levels. (c) Same ratios as in panel (b) but for the 2^+_1 level in ^{208}Pb, for (p, p) (red curves) and (n, n') (black curves). Ratios including (full curves) or excluding (dashed curves) the isovector part of rearrangement corrections are displayed.

1-30 MeV, accounting for rearrangement reduces the cross section leads to reduced inelastic cross sections magnitudes of 30% to 55%. We note that, for $L \geqslant 4$, the impact of rearrangement noticeably decreases as the transition multipolarity increases.

The rearrangement corrections also depend on the nature of the excitations considered. As an illustration, we display in Fig. 11(b) the ratios $\frac{\sigma_R}{\sigma_0}$ for neutron and proton inelastic scatterings to the 2^+_1 and $2^+_{\text{IS-SV}}$ levels in ^{206}Pb. Impact of rearrangement on the proton inelastic cross section vanished as we move beneath the Coulomb barrier, since the nuclear component of the transition potential becomes negligible in front of the Coulomb component, thus leading to a ratio $\frac{\sigma_R}{\sigma_0} = 1$. We observe that rearrangement effects on the neutron inelastic cross sections for the 2^+_1 and $2^+_{\text{IS-SV}}$ levels (compare the black full and dashed curves) are very similar. This is understood considering that (i) incident neutron mainly probes proton densities and (ii) the proton transition densities to these two levels have a very similar shape. In contrast, for proton scattering, a difference between rearrangement effects between the 2^+_1 and $2^+_{\text{IS-SV}}$ levels is seen. Indeed, as incident proton mainly probes neutron densities at these energies, the different nature of the two corresponding neutron transition densities [see Figs. 9(a) and 9(c)] induces differences in size of the rearrangement correction.

We finally display in Fig. 11(c) the inelastic cross section ratios, in the case of the 2^+_1 excited level in ^{208}Pb, for both neutron and proton inelastic scattering, for rearrangement including only isoscalar terms [label $R = R_0$, second line of Eq. (7)], and for rearrangement of both isoscalar and isovector terms [label $R = R_0 + R_1$, whole Eq. (7)]. In our calculations for ^{208}Pb, we note that the impact of rearrangement is minimum at proton incident energies of 130 MeV. Similar behavior was observed for other low-lying excitations in ^{208}Pb. Moreover, Fig. 11(c) shows that the isovector part of the rearrangement component plays an important role as neglecting them would result in a cross section approximately 10% higher than that for the complete calculations [in Fig. 11(c), compare red full curve to red dashed curve for proton scattering, and black full curve to dashed black curve for neutron scattering].

In sum, depending on the nature of the transition, its isospin character, the probe, and incident energy, the impact of rearrangement corrections to the inelastic cross section strongly varies. Calculations omitting these corrections would result in incorrect prediction of the cross-section magnitude. A comprehensive analysis of the impact of rearrangement terms on nucleon scattering properties will be reported in a forthcoming paper.

E. Analysis of differerential inelastic (n, n') data

Comparisons between experimental data and calculated cross sections from models A and B are displayed in Figs. 5 to 8 for various low-energy excitations:

(i) ^{206}Pb: (n, n') scattering from the 2^+_1 [see Figs. 5(a) and 5(b)] and 3^-_1 [see Fig. 5(c)] levels;

(ii) ^{207}Pb: scattering from the ($5/2^+$-$7/2^+$) multiplet [see Figs. 6(a) and 6(b)];

(iii) ^{209}Bi: scattering from the ($3/2^+$-$15/2^+$) multiplet [see Fig. 6(c)];

(iv) ^{208}Pb: scattering from the 3^-_1 level [see Figs. 7(a)–7(c)];

(v) ^{208}Pb: scattering from the 5^-_1 [see Figs. 10(d) and 10(e)] and 2^+_1 [see Fig. 7(f)] levels; and

(vi) ^{208}Pb: scattering from the (2^+_1, 4^+_1, 6^+_1) triplet and (4^+_1, 6^+_1) doublet [see Figs. 8(a) and 8(b), respectively].

In those figures, the new experimental cross sections are displayed as open blue triangles. The full red curves are results from model A, and the dashed black curves are for the calculations performed within model B.

The overall shape and magnitude of the measurements are well reproduced by model A, though we can see a few discrepancies. These are closely discussed for the $L = 3$ transitions in the four nuclei in Sec. VII F 1, and for the 2^+_1 state in ^{206}Pb in Sec. VII F 2. For ^{208}Pb, we display in Fig. 8 the comparison of the new data to our calculation for the sum of the contributions from the 2^+_1, 4^+_1, and 6^+_1 states [Fig. 8(a)], or from the contributions of the 4^+_1 and 6^+_1 states [Fig. 8(b)]. Our calculations are in quite good agreement with the present data. We emphasize that the rearrangement corrections reduce the inelastic cross section by an amount between 30% and

55%, as seen in Sec. VII D. The overall good agreement of our calculations with measurements seen in Figs. 5 to 8 for incident neutrons is then strongly connected to the account of such corrections.

Note that experimental data for group of levels in various energy excitation ranges between 3.92 and 4.48 MeV were previously reported [58]. However, these data are at least three times larger than the calculations we performed considering the group of levels indicated in the Appendixes of Ref. [58]. It is likely that these data suffer from inaccurate background subtraction and/or contamination from an other element, considering the abnormal rise of the inelastic spectrum for excitation energies above 3 MeV (see Fig. 1 of Ref. [58]). We therefore excluded these data sets from our analysis.

Calculations performed within model B are mostly comparable in quality to our microscopic calculations (model A), though they appear to be slightly worse in some specific cases. Adjusting the deformation parameters, namely allowing $\beta_L^{(n,n')} \neq \beta_L^{(C)}$, as well as allowing different deformations for the various potential components would obviously improve their quality, as was done in many studies before. However, this comparison to the collective model calculations highlights the accuracy of the present microscopic calculations for this extended set of inelastic scattering data, since it is able to account for the main features of all direct inelastic scattering cross sections without any normalization procedure or prior knowledge of reduced transition probabilities.

F. Discussion

This section is dedicated to the detailed review of experiment-theory mismatches for the octupole transition in the four considered targets [Sec. VII F 1] and for the yrast 2^+ level excitation in ^{206}Pb [Sec. VII F 2]. For this last case, in view of the surprising disagreement between modeled and measured cross sections, various aspects of the modeling are discussed in Sec. VII F 3.

1. The 3_1^- state in ^{206,208}Pb and first octupole multiplet of ^{207}Pb and ^{209}Bi

For the 3_1^- excitations in ^{206,208}Pb, and the corresponding first octupole multiplet of ^{207}Pb and ^{209}Bi, experimental data sets are compared to calculations in Fig. 5(c) for ^{206}Pb, Figs. 6(a) and 6(b) for ^{207}Pb, Fig. 6(c) for ^{209}Bi, and Figs. 7(a)–7(c) for ^{208}Pb. For ^{207}Pb, one data set at 13.7 MeV [black symbols on the 13.5-MeV results, Fig. 6(b)] is above the calculation and the new data set from this work. Our calculations are in good agreement with the new data sets which are consistent in the energy range 10–15 MeV. This seems to indicate that the 13.7-MeV ^{207}Pb data normalization is slightly off.

For ^{206}Pb, two data sets of Hicks *et al.* at 4.6 and 8.01 MeV [45] [full black squares in Fig. 5(c)] are larger than the calculations, while calculations agree with other data sets in the 6- to 13.5-MeV range. Note that in Fig. 5(c), the data set at 8.01 MeV of Hicks *et al.* disagrees with that of Kinney *et al.* at 8 MeV [58] (open black circles), which falls on our calculation.

We also note that the 3.96-MeV 3_1^- data for ^{208}Pb [94] [Fig. 7(a)] and the 3.56-MeV data for the $(5/2^+$-$7/2^+)$ multiplet in ^{207}Pb [96] [Fig. 6(a)] are above the calculations as well. However, the 3.06- and 3.55-MeV data for the $(3/2^+$-$15/2^+)$ multiplet in ^{209}Bi [Fig. 6(c)] are well accounted for by the present approach.

Considering the global agreement between our model predictions and most of the experimental data for various excited states in various targets in the whole energy range of the present study, and the expected smooth variation in energy of the inelastic cross sections magnitude, it is likely that the cross-section magnitudes of the data sets at 4.6 and 8.01 MeV [45] for ^{206}Pb [Figs. 5(b) and 5(c)], at 3.56 for the multiplet in ^{207}Pb [Fig. 9(a)], and at 3.96 MeV [94] [Fig. 6(a)] and 13.7 MeV [93] [Fig. 7(c)] in ^{208}Pb may display a normalization issue.

We note that our calculations underestimate the data in the 15.5- to 26-MeV energy range for the 3_1^- excitation in ^{208}Pb. A small mismatch with elastic neutron scattering data is also observed in the same energy range. The coupled channel calculations we performed (not shown), accounting for the coupling between the elastic and the inelastic 3_1^- channels, cannot explain these disagreements.

2. ^{206}Pb(n, n') 2_1^+

For the ^{206}Pb(n, n') 2_1^+ reaction, a large discrepancy at angles below 90° between neutron data and calculations is found at the four incident energies, 4.6, 8.01, 11.5, and 13.5 MeV [see Fig. 5(b)]. However, the data sets below 4.02 MeV in ^{206}Pb [see Fig. 5(a)] are well reproduced by the present model. This supports our claim that compound nuclear processes, which are dominant below 4 MeV for this nucleus, are well accounted for.

3. Interpretation of the ^{206}Pb $(n, n')2_1^+$ data

For the ^{206}Pb(n, n') 2_1^+ case, one may wonder if the experience-theory mismatch above 4 MeV may come from inaccuracies in our direct reaction modeling with model A. These could be related to (i) the nuclear structure ingredients, namely QRPA neutron and proton transition densities, (ii) the JLM-B folding model and its inherent approximations, such as the use of local potentials, or (iii) the application of the DWBA approximation. Similar discrepancies between measurements and model B calculations are observed. To help understand this mismatch, we review below these various features of the present modeling [Secs. VII F 3 a to VII F 3 d]. Finally, we end with a very general remark on possible experimental difficulties related to the ^{206}Pb$(n, n')2^+$ cross-section measurements.

a. Proton inelastic scattering off ^{206}Pb. To further assess the validity of the present reaction modeling and the QRPA nuclear structure input, we extended our analysis to proton inelastic scattering off ^{206}Pb. We compare our microscopic model predictions (full red curves) to available experimental data in Fig. 12 for the 2_1^+ state and other low-lying states in ^{206}Pb, namely 3_1^-, 4_1^+, 5_1^-, 7_1^-, and $2_{\text{IS-SV}}^+$. Nuclear structure properties for these excitations are well described within the QRPA approach, as discussed in Sec. IV (see Tables VI

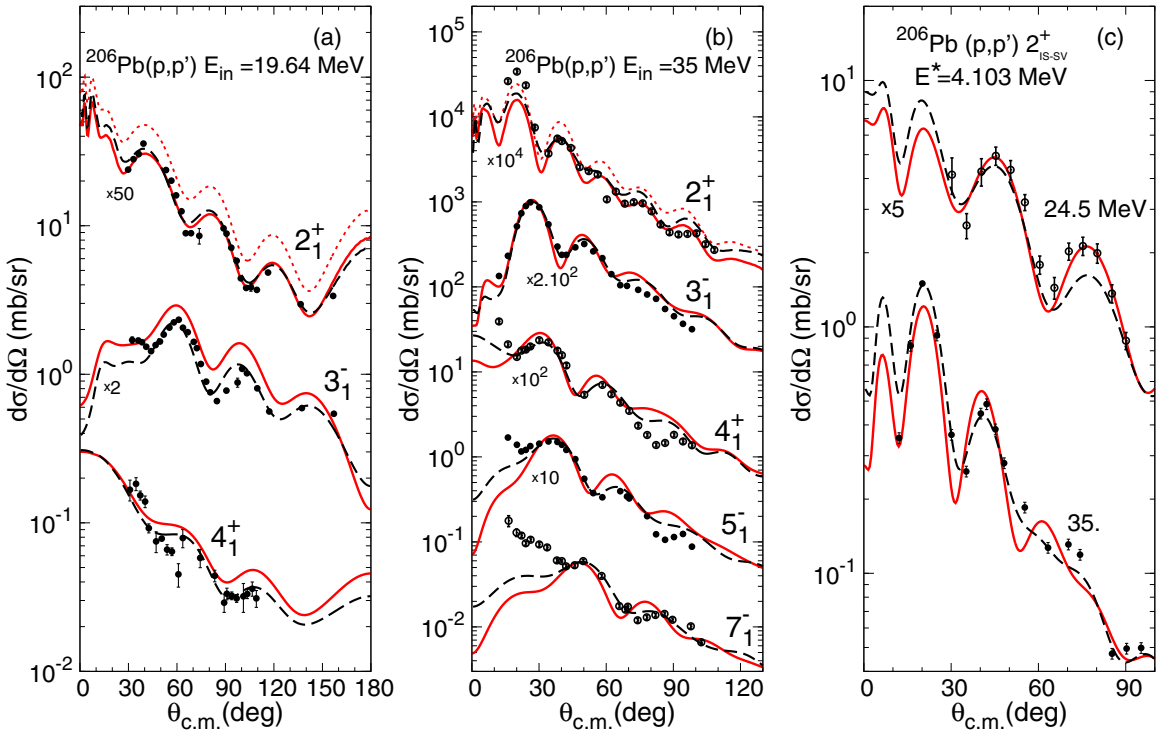

FIG. 12. Differential cross sections for proton inelastic scattering off ^{206}Pb at 19.64 MeV [panel (a)] and 35 MeV [panel (b)]. In panels (a) and (b), spins, parities, and excitation energies are indicated on each plots. (c) Same reaction for the $2^{+}_{\text{IS-SV}}$ level located at $E^{*} = 4.102$ MeV. Incident energies are indicated on the plot. On the three panels, symbols represent experimental values at energies 19.64, 24.5, and 35 MeV from Refs. [136–138], respectively. JLM-B calculations with HFB/QRPA matter and transition densities are plotted as full red curves. Dotted red curves represent calculations for the 2^{+}_{1} level for which the M_n value was multiplied by a factor 1.257 (see discussion of Sec. VII F 2). Dashed black curves are calculations from the collective model with the deformation parameters indicated in the last column of Table VIII.

and VII). Calculations performed within the collective model [Sec. V] are displayed as dashed black curves. In that case, the nuclear deformation parameters, fitted to reproduce the various proton angular distributions, are indicated in Table VIII (see right column labeled $\beta_L^{(p,p')}$). The charge deformation calculated from empirical $B(EL)$ values [or from QRPA $B(EL)$ value for the 5^{-}_{1} state] was used for Coulomb excitation (see Table VIII, column labeled β_L).

The overall agreement between the JLM-B/QRPA calculation and the measurements is very good. For the incident energy 35 MeV [Fig. 12(b)], the 7^{-} data are higher than the calculations at forward angle. This is also the case, but to a lesser extent, for the 5^{-}_{1} and 4^{+}_{1} states [Fig. 12(b)]. The 2^{+}_{1} state (p, p') data at 19.64 MeV [Fig. 12(a)] are very well reproduced, but the first peak below 30° at 35 MeV is underestimated by the calculation. Note that similar mismatches are obtained when comparing our empirical calculations from the collective model (black long-dashed curves) to the measurements. The 3^{-}_{1} state (p, p') data at 19.64 MeV [Fig. 12(a)] are below our JLM-B/QRPA calculation, which is surprising since (i) the 35 MeV data are well reproduced, (ii) the predicted $B(E3\uparrow)$ agrees very well with the empirical one (see Table VI), and (iii) for this isoscalar excitation, the neutron transition density is N/Z times the proton transition density ($M_n/M_p \simeq N/Z$, see Table VII); thus, the proton scattering magnitude, as protons mainly probe the neutron density, should be reproduced within our microscopic model. Considering now the $2^{+}_{\text{IS-SV}}$ state at 4.102 MeV, the predicted JLM-B/QRPA angular distributions agree very well with measurements at 24.5 and 35 MeV [Fig. 12(c)]. This state is identified to the main isoscalar surface vibration mode ($M_n/M_p \simeq N/Z$, see Table VII) and has the same nature as that for the yrast 2^{+} state in ^{208}Pb. The agreement between measurements and the collective model calculation at 24.5 MeV is slightly worse, especially at angles above 70°.

In sum, in ^{206}Pb, these comparisons between experimental data, calculations from the collective model with empirical nuclear deformation parameters, and our JLM-B/QRPA predictions, show that our microscopic modeling provides a satisfactory description of proton inelastic scattering data, including that for the 2^{+}_{1} level.

b. Neutron and proton matrix elements. We showed in Sec. IV that the charge transition densities are quite well reproduced for these state (see Fig. 9 and Table VI). Proton inelastic cross sections are sensitive to both the neutron and proton transition densities but the spin-independent two-body force between unlike nucleons is stronger than the force between alike nucleons: The neutron-proton interaction is about three times larger that the neutron-neutron interaction in the 10- to 50-MeV energy range [125]. For these various states, the agreement between the (p, p') data and our calculations shows that the present QRPA neutron transition densities are realistic. Moreover, for the 2^{+}_{1} level, the ratio R_{np} [see Eq. (17)] values inferred from pion, proton, and

ion inelastic scattering measurements, as well as previous (Q)RPA calculations (see details and references in Table VII), are in the range 1.28–1.76 (considering the high part of error bars) and are compatible with the present QRPA/D1S value of $R_{np} = 1.4$. We scaled the QRPA neutron radial transition densities by a factor $1.76/1.4 \simeq 1.257$ so as to fit the extreme empirical R_{np} values of 1.76 and check the impact of these two calculation on (n, n') and (p, p') results. This leads to a uniform increase (not shown) of the (n, n') cross section by $\approx$22% for $E_{\rm in} = 8$, 11.5, 13.5 MeV and 11% for $E_{\rm in} = 4.6$ MeV. The lower energy cross sections are less impacted as they contain a large inelastic compound contribution. It is hard to state if these changes could improve the agreement between our calculations and the measurements, considering (i) the large experimental uncertainties, (ii) the possible overall normalization issue in the available (n, n') measurements, especially at 4.6 and 8 MeV as discussed in Sec. II B 1, and (iii) that the calculations would have to be scaled by a factor 4 to 8 to reproduce the reported measurements at angles below 90°. For (p, p'), scaling the M_n value increases the cross section by about 58% [dashed red curves in Figs. 12(a) and 12(b)]. This factor corresponds to the square of the M_n value increase, which is easily understood considering that a proton projectile mainly probes the neutron density. This leads to a strong overestimation of the measurements at 24.5 MeV. At 35 MeV, even if this scaling improves the agreement at angle below 30°, it leads to a strong overestimation of the measurement in the 30–100° angular range. This seems to indicate that the predicted QRPA value of $R_{np} \simeq 1.4$ is realistic as a significant increase of this value strongly undermines the overall good agreement with available (p, p') data.

In sum, we have various strong arguments to consider that both proton and neutron transition densities are well described for the 2_1^+ state in ^{206}Pb by the present QRPA calculation. The discrepancies observed between measurements and calculations for neutron inelastic scattering is therefore not likely related to inadequate nuclear structure inputs.

c. Local potentials. One shortcoming of the present model is related to the use of local potentials while it is well known that optical and transition potentials are nonlocal. However, our local representation of these potentials gives quite accurate results for most of transitions studied here. Moreover, previous studies have shown that nonlocal effect, such as the Perey effect, would be small for an inelastic form factor strongly peaked at the nuclear surface [139]. Besides, a previous calculation [140] of the reaction ^{206}Pb(p, p') to the 2_1^+ level including nonlocality within the Perey approximation, in which the distorted wave functions are first calculated with a local potential and then damped in the nuclear interior [141], displays a reduction of the inelastic cross section at angles below 60° of about 25%. This illustrates the extent of the impact of nonlocal corrections on inelastic cross section, which is too small, and has the wrong sign, to explain the large discrepancies between measurements and our calculations as observed in Fig. 5(b).

d. DWBA approximation. Finally, going beyond the DWBA approximation by accounting for coupled channel effects would result in small changes in the inelastic cross section. The explicit couplings between the elastic and some inelastic channels would necessitate, at least, decreasing the imaginary part of our optical potential, thus of the JLM-B effective interaction, to account for the loss of flux in the elastic channel. However, the induced modifications on the optical potential, and thus on the distorted waves, are almost completely compensated by the change needed in the interaction from which transition potential are determined, so the net impact on inelastic cross section is very weak.

e. Separating elastic from inelastic peaks in TOF spectra for ^{206}Pb$(n.n')2_1^+$. The 2_1^+ state in ^{206}Pb lies at 0.803 MeV and its expected (n, n') inelastic cross sections are quite small, considering the predicted small $B(E2\uparrow) = 8.2$ Weisskofp units. These conditions did not make the threshold extraction process easy, especially for the elastic component from multiple scattering, in the experimental spectra analyses. Actually, a contamination of the 2^+ inelastic peak with a small amount of the huge elastic peak might explain the unusually sharp rise observed in (n, n') scattering cross sections at angles below 90°. This possibility remains to be checked.

In sum, after the thorough review of various aspects of the models, the sharp rise of the ^{206}Pb(n, n') 2_1^+ differential cross section measurements at angles below 90° for incident energies between 4.6 and 13.5 MeV remains puzzling. New neutron scattering measurements could help alleviating or curing present deficiencies. From a scattering model perspective, it might also be worth extending the scattering model from DWBA to the coupled-channel (CC) formalism, in which care would be taken of an explicit coupling between the 2_1^+ and 3_1^- levels in ^{206}Pb, as suggested by the electric dipole $(3_1^- \rightarrow 2_1^+)$ transition observed in the γ-decay properties of excited states in this Pb isotope [117]. Such CC calculations are out of the scope of the present work.

VIII. SUMMARY AND CONCLUSIONS

New neutron elastic and inelastic scattering measurement are reported for the four target ^{206,207,208}Pb and ^{209}Bi. These measurements have been carried out about three decades ago [24,25], and most of the data obtained at that time has not been published yet. Pulsed beam of deuterons delivered by the super EN tandem van de Graaff accelerator was incident on a deuterium gas cell to produce, by the ^{2}H$(d, n)^3$He reaction, monoenergetic neutrons in the 7.5- to 15.5-MeV energy range. The neutrons were then scattered from a small sample of Bi and highly enriched samples of ^{207,209,209}Pb into an array of four detectors. For each sample and each energy, data were taken at 29 angles between 20° and 160° in steps of 5°, with nine settings of the detector array. Scattered neutron energies were determined via TOF techniques. The settings were arranged so that for each set of angles at least one previous data-collection angle was repeated to assure consistency of the data between the different angle sets. The results obtained in our laboratory and presented in this paper contribute largely to complete our knowledge on fast-neutron scattering from nuclei in the region of the doubly magic shell $A = 208$.

An analysis of the measurement cross section based on the JLM-B folding model was performed. Ground-state and

transition radial neutron and proton densities were obtained within Hartree-Fock-Bogoliubov and quasiparticle random phase approximation approaches implemented with the Gogny D1S interaction for ^{206,208}Pb. The weak coupling approximation was applied to describe excitation process of the $L = 3$ multiplets in ^{207}Pb and ^{209}Bi. The overall results are in very good agreement with measurements in the 4- to 27-MeV region for which all published neutron differential data to our knowledge were analyzed. The only phenomenological inputs are the Gogny D1S interaction for nuclear structure and the JLM-B effective interaction. Parameters of the JLM-B interaction were fitted in a previous work on nucleon elastic scattering and charge exchange observables and were not changed in the present analysis.

For inelastic scattering, the Cheon rearrangement correction is accounted for and is shown to reduce the calculated cross section up to 55%, while its impact varies greatly with the incident energy and the multipole transfer value. The overall good agreement between our inelastic scattering calculations with measurements could not have been achieved without those corrections.

The combined analysis of nuclear structure properties, reduced and radial transition probabilities, neutron-to-proton moment ratios, and neutron and proton inelastic cross sections allows to identify specific experimental data that presumably need revision. Data sets that may present some normalization and/or background subtraction issues are those for the 3_1^- excitation at 4.6 and 8.01 MeV [45] for ^{206}Pb, at 3.06 and 3.55 MeV for the multiplet in ^{209}Bi, and at 3.96 MeV in ^{208}Pb, as well as those for the yrast 2^+ state in ^{206}Pb, at 4.6 and 8.0 MeV [45] and at 11.5 and 13.5 MeV (present work). Our analysis will help to define a better set of data to both constrain phenomenological models and challenge microscopic and *ab initio* models which are nowadays widely developed. However, as nuclear reaction models can always be questioned, it would be of great interest to perform new measurements whenever theory and experiment cannot agree, even for nucleon scattering on stable isotopes. For instance, for neutron inelastic scattering to the yrast 2^+ excitation above 4 MeV, the systematic mismatch between calculations and measurements highlighted in the present work calls for new experiments and a refinement of the reaction theory.

Finally, in light of the extent of the rearrangement corrections found in the present analysis within the JLM-B folding model extended to inelastic scattering process, it would be relevant to study the form these corrections should take in the context of a full-folding model with *g*-matrix solutions of Brueckner-Bethe-Goldstone equations [142,143] that provides nonlocal potentials in coordinate space and their impact on scattering observables predicted from this theory. Neglecting rearrangement corrections may lead to inaccurate conclusions when nuclear structure properties, such as neutron-to-proton matrix elements ratio, are inferred from hadron scattering studies within microscopic reaction models built from density-dependent effective interactions. A review of nuclear structure properties inferred from scattering studies with various probes thus may be needed.

ACKNOWLEDGMENTS

One of the authors (M.D.) would like to thank S. Péru for her assistance with the axially deformed QRPA code and S. Hilaire for constructive criticism of the manuscript. The above presented experimental work would not have been achieved without the helpful collaboration of the members of the "Fast-neutron-scattering" group of Bruyères-le-Châtel, namely S. Seguin, who was in charge of design and operation of the neutron source; C. Humeau (deceased), to whom was entrusted the responsibility of the whole electronics of the data-acquisition setup; J. P. Lochard, who handled the heavy shielding ensemble and took care of the numerous alignment operations; and J. Chardine, whose job was to analyze the recorded time-of-flight spectra in order to obtain the differential cross sections. This work has also benefited of the help of R. Shamu (deceased) (Western Michigan University, Kalamazoo, USA), on sabbatical in our laboratory during data collection, and Y. Patin and J. Sigaud, who provided us with informed advice and constructive discussions about TOF metrology at our laboratory.

[1] G. R. Satchler, *Direct Nuclear Reactions* (Oxford University Press, Oxford, 1983).
[2] V. Semkova, N. Otuka, M. Mikhailiukova, B. Pritychenko, and O. Cabellos, EPJ Web Conf. **146**, 07003 (2017).
[3] A. J. Koning, Tech. Rep. NEA/DB/DOC(2014)3, OECD, NEA Data Bank (2014), http://www.oecd-nea.org/databank/docs/2014/.
[4] G. Berton, G. Damart, O. Cabellos, B. Beauzamy, N. Soppera, and M. Bossant, EPJ Web Conf. **146**, 06030 (2017).
[5] A. J. Koning and D. Rochman, Nucl. Data Sheets **113**, 2841 (2012).
[6] J.-P. Jeukenne, A. Lejeune, and C. Mahaux, Phys. Rev. C **16**, 80 (1977).
[7] S. Mellema, R. W. Finlay, and F. S. Dietrich, Phys. Rev. C **33**, 481 (1986).
[8] E. Bauge, J. P. Delaroche, and M. Girod, Phys. Rev. C **58**, 1118 (1998).
[9] J. Klug, J. Blomgren, A. Atac, B. Bergenwall, A. Hildebrand, C. Johansson, P. Mermod, L. Nilsson, S. Pomp, U. Tippawan *et al.*, Phys. Rev. C **67**, 031601(R) (2003).
[10] J. H. Osborne, F. P. Brady, J. L. Romero, J. L. Ullmann, D. S. Sorenson, A. Ling, N. S. P. King, R. C. Haight, J. Rapaport, R. W. Finlay *et al.*, Phys. Rev. C **70**, 054613 (2004).
[11] A. Öhrn, J. Blomgren, P. Andersson, A. Ataç, C. Gustavsson, J. Klug, P. Mermod, S. Pomp, P. Wolniewicz, M. Österlund *et al.*, Phys. Rev. C **77**, 024605 (2008).
[12] C. Lagrange and J. C. Brient, J. Phys. (Paris) **44**, 27 (1983).
[13] L. F. Hansen, B. A. Pohl, C. Wong, R. C. Haight, and C. Lagrange, Phys. Rev. C **34**, 2075 (1986).
[14] E. Bauge, J. Delaroche, and M. Girod, Nucl. Phys. A **654**, 829c (1999).

[15] E. Khan, T. Suomijärvi, Y. Blumenfeld, N. V. Giai, N. Alamanos, F. Auger, E. Bauge, D. Beaumel, J. Delaroche, P. Delbourgo-Salvador *et al.*, Nucl. Phys. A **694**, 103 (2001).

[16] F. S. Dietrich, J. D. Anderson, R. W. Bauer, S. M. Grimes, R. W. Finlay, W. P. Abfalterer, F. B. Bateman, R. C. Haight, G. L. Morgan, E. Bauge *et al.*, Phys. Rev. C **67**, 044606 (2003).

[17] M. Dupuis, E. Bauge, S. Hilaire, F. Lechaftois, S. Péru, N. Pillet, and C. Robin, Eur. Phys. J. A **51**, 168 (2015).

[18] V. Lapoux and N. Alamanos, Eur. Phys. J. A **51**, 91 (2015).

[19] A. Corsi, S. Boissinot, A. Obertelli, P. Doornenbal, M. Dupuis, F. Lechaftois, M. Matsushita, S. Péru, S. Takeuchi, H. Wang *et al.*, Phys. Lett. B **743**, 451 (2015).

[20] M. L. Cortés, P. Doornenbal, M. Dupuis, S. M. Lenzi, F. Nowacki, A. Obertelli, S. Péru, N. Pietralla, V. Werner, K. Wimmer *et al.*, Phys. Rev. C **97**, 044315 (2018).

[21] D. K. Srivastava and H. Rebel, J. Phys. G **10**, L127 (1984).

[22] T. Cheon, K. Takayanagi, and K. Yazaki, Nucl. Phys. A **437**, 301 (1985).

[23] T. Cheon, K. Takayanagi, and K. Yazaki, Nucl. Phys. A **445**, 227 (1985).

[24] G. Haouat, O. Bersillon, J. Lachkar, Y. Patin, and C. Lagrange, CEA report No. CEA-N-2200 (France), 1982.

[25] G. Haouat, F. Dietrich, Y. Patin, R. De Swiniarski, C. Humeau, J. Chardine, J. P. Lochard, and S. Seguin, CEA report No. CEA-N-2284 (France), 1982.

[26] C. Lagrange and M. Girod, J. Phys. G **9**, L97 (1983).

[27] S. Péru and H. Goutte, Phys. Rev. C **77**, 044313 (2008).

[28] S. Péru, G. Gosselin, M. Martini, M. Dupuis, S. Hilaire, and J.-C. Devaux, Phys. Rev. C **83**, 014314 (2011).

[29] A. Adam and J. Cabé, Nucl. Inst. Methods **121**, 339 (1974).

[30] J. Lachkar, M. T. Mc Ellistrem, G. Haouat, Y. Patin, J. Sigaud, and F. Coçu, Phys. Rev. C **14**, 933 (1976).

[31] G. Haouat, J. Lachkar, J. Sigaud, Y. Patin, and F. Coçu, Nucl. Sci. Eng. **65**, 331 (1978).

[32] G. Haouat, J. Lachkar, C. Lagrange, J. Jary, J. Sigaud, and Y. Patin, Nucl. Sci. Eng. **81**, 491 (1982).

[33] Precision Foils Division, Hamilton Technology, Lancaster, PA, USA.

[34] L. Cranberg, A. H. Armstrong, and R. L. Henkel, Phys. Rev. **104**, 1639 (1956).

[35] G. F. Bogdanov, N. A. Vlasov, S. P. Kalinin, B. V. Ryakov, and V. A. Sydorov, Sov. Phys. JETP **3**, 793 (1956).

[36] H. W. Lefevre, R. R. Borchers, and C. H. Poppe, Phys. Rev. **128**, 1328 (1963).

[37] E. Bauge, J. P. Delaroche, and M. Girod, Phys. Rev. C **63**, 024607 (2001).

[38] E. Bauge, J. P. Delaroche, M. Girod, G. Haouat, J. Lachkar, Y. Patin, J. Sigaud, and J. Chardine, Phys. Rev. C **61**, 034306 (2000).

[39] T. B. Clegg, G. Haouat, J.-P. Delaroche, C. Lagrange, J. Chardine, M. T. Mc Ellistrem, S. E. Hicks, and G. R. Shen, Phys. Rev. C **40**, 2527 (1989).

[40] W. E. Kinney, Nucl. Instrum. Methods **83**, 15 (1970).

[41] G. Haouat, C. Lagrange, J. C. Brient, Y. Patin, and R. De Swiniarski, in *Proceedings of the Conference on Nucleon-Nucleus Collisions, a Probe of Nuclear Structure*, edited by J. Rapaport, R. W. Finlay, S. M. Grimes, and F. S. Dietrich, AIP Conf. Proc. No. 124 (AIP, New York, 1985), p. 208.

[42] R. Schamu, J. Barnes, S. Fergusson, G. Haouat, and J. Lachkar, J. Phys. G **17**, 525 (1991).

[43] N. Olsson, B. Holmqvist, and E. Ramström, Nucl. Phys. A **385**, 285 (1982).

[44] P. L. Okhuysen and J. T. Prud'homme, Phys. Rev. **116**, 986 (1959).

[45] S. F. Hicks, J. M. Hanly, S. E. Hicks, G. R. Shen, and M. T. Mc Ellistrem, Phys. Rev. C **49**, 103 (1994).

[46] S. C. Buccino, C. E. Hollandsworth, and P. R. Bevington, Z. Phys. **196**, 103 (1966).

[47] M. A. Etemad, B. Holmqvist, and T. Wiedling, Tech. Rep. 482, Aktiebolaget Atomenergi, Stockholm/Studsvik Repts., 1973.

[48] D. B. Thomson, Phys. Rev. **129**, 1649 (1963).

[49] C. D. Zafiratos, T. A. Oliphani, J. S. Levin, and L. Cranberg, Phys. Rev. Lett. **14**, 913 (1965).

[50] B. Holmqvist, T. Wiedling, and M. Salama, Tech. Rep. 430, Aktiebolaget Atomenergi, Stockholm/Studsvik Repts., 1971.

[51] J. C. Ferrer, J. D. Carlson, and J. Rapaport, Nucl. Phys. A **275**, 325 (1977).

[52] G. E. Belovitskii, L. N. Kolesnikova, and I. M. Frank, Yad. Fiz. **15**, 662 (1972) [Sov. J. Nucl. Phys. **15**, 369 (1972)].

[53] N. Olsson, B. Trostell, E. Ramstroem, and B. Holmqvist, Nucl. Phys. A **472**, 237 (1987).

[54] R. B. Day, EXFOR accession no. 12191011, 1965.

[55] P. T. Guenther, D. G. Havel, and A. B. Smith, Nucl. Sci. Eng. **65**, 174 (1978).

[56] J. L. Fowler, Phys. Rev. **147**, 870 (1966).

[57] J. R. M. Annand, R. W. Finlay, and F. S. Dietrich, Nucl. Phys. A **443**, 249 (1985).

[58] W. E. Kinney and F. G. Perey, Tech. Rep. 4909, Oak Ridge National Laboratory Reports, 1974.

[59] J. Rapaport, T. S. Cheema, D. E. Bainum, R. W. Finlay, and J. D. Carlson, Nucl. Phys. A **296**, 95 (1978).

[60] M. L. Roberts, P. D. Felsher, G. J. Weisel, Z. Chen, C. R. Howell, W. Tornow, R. L. Walter, and D. J. Horen, Phys. Rev. C **44**, 2006 (1991).

[61] J. P. Delaroche, C. E. Floyd, P. P. Guss, R. C. Byrd, K. Murphy, G. Tungate, and R. L. Walter, Phys. Rev. C **28**, 1410 (1983).

[62] C. E. Floyd Jr., Ph.D. thesis, Duke University, Durham, NC, 1981.

[63] L. F. Hansen, F. S. Dietrich, B. A. Pohl, C. H. Poppe, and C. Wong, Phys. Rev. C **31**, 111 (1985).

[64] R. W. Finlay, J. R. M. Annand, T. S. Cheema, J. Rapaport, and F. S. Dietrich, Phys. Rev. C **30**, 796 (1984).

[65] R. D. Lawson, P. T. Guenther, and A. B. Smith, Phys. Rev. C **36**, 1298 (1987).

[66] X. Wang, Y. Wang, D. Wang, and J. Rapaport, Nucl. Phys. A **465**, 483 (1987).

[67] J. R. Beyster, M. Walt, and E. W. Salmi, Phys. Rev. **104**, 1319 (1956).

[68] S. P. Simakov, G. N. Lovchikova, O, A, Sal'nikov, G. V. Kotel'nikova, and A. M. Trufanov, USSR Report No. 197 (INDC, Austria, 1982), p. 17.

[69] B. Holmqvist, T. Wiedling, S. G. Johansson, G. Lodin, A. Kiss, B. Gustavsson, and B. Antolkovic, Tech. Rep. 366, Aktiebolaget Atomenergi, Stockholm/Studsvik Repts., 1969.

[70] R. K. Das and R. W. Finlay, Phys. Rev. C **42**, 1013 (1990).

[71] A. H. Hussein, J. M. Cameron, S. T. Lam, G. C. Neilson, and J. Soukup, Phys. Rev. C **15**, 233 (1977).

[72] W. Bucher and C. E. Hollandsworth, Phys. Lett. B **58**, 277 (1975).
[73] P. H. Stelson, R. L. Robinson, H. J. Kim, J. Rapaport, and G. R. Satchler, Nucl. Phys. **68**, 97 (1965).
[74] J. O. Elliot, Phys. Rev. **101**, 684 (1956).
[75] L. A. Rayburn, Phys. Rev. **116**, 1571 (1959).
[76] L. Rosen and L. Stewart, Phys. Rev. **107**, 824 (1957).
[77] G. Deconninck, A. Martegani, J. P. Meulders, and J. Stoquart, Ann. Soc. Sci. Bruxelles. Ser. I **75**, 102 (1961).
[78] M. Matoba, M. Hyakutake, H. Tawara, K. Tsuji, H. Hasuyama, S. Matsuki, A. Katase, and M. Sonoda, Nucl. Phys. A **204**, 129 (1973).
[79] A. Takahashi, M. Gotoh, Y. Sasaki, and H. Sugimoto, Tech. Rep. 92, Osaka University, OKTAVIAN Reports, 1992.
[80] K. Yuasa, J. Phys. Soc. Jpn. **13**, 1248 (1958).
[81] M. Gonggui, Z. Yiming, X. Daquan, W. Shiming, L. Jingde, and C. Shuying, Chinese report to the I.N.D.C., No. 11, p. 135 (1988), Austria.
[82] V. I. Strizhak, V. V. Bobyr, and L. Y. Grona, Sov. Phys. JETP **14**, 225 (1962).
[83] W. G. Cross and R. G. Jarvis, Nucl. Phys. **15**, 155 (1960).
[84] P. Kuijper, J. C. Veefkind, and C. C. Jonker, Nucl. Phys. A **181**, 545 (1972).
[85] C. I. Hudson, W. S. Walker, and S. Berko, Phys. Rev. **128**, 1271 (1962).
[86] R. Finlay, W. Walter, A. Marcinkowski, and J. Rapaport (private communication to EXFOR, accession number 13532003).
[87] T. P. Stuart, J. D. Anderson, and C. Wong, Phys. Rev. **125**, 276 (1962).
[88] H. H. Landon, A. J. Elwyn, G. N. Glasoe, and S. Oleksa, Phys. Rev. **112**, 1192 (1958).
[89] E. Poenitz, R. Nolte, D. Schmidt, and G. Chen, J. Korean Phys. Soc. **59**, 1876 (2011).
[90] L. Cranberg, T. A. Oliphant, J. Levin, and C. D. Zafiratos, Phys. Rev. **159**, 969 (1967).
[91] E. Poenitz, R. Nolte, and D. Schmidt, in *Proceedings of the International Conference on Nuclear Data for Science and Technology, Nice, France, April 22–27, 2007*, edited by O. Bersillon, F. Gunsing, E. Bauge, R. Jacqmin, and S. Leray (EDP Sciences, 2008), p. 513.
[92] M. Abdel-Harith, Th. Schweitzer, D. Seeliger, and S. Unholzer, Zentralinst. f. Kernforschung Rossendorf Reports, No. 315, (Germany), 1976, p. 12.
[93] G. E. Belovitskii, L. N. Kolesnikova, and I. M. Frank, Yad. Fiz. **15**, 666 (1972) [Sov. J. Nucl. Phys. **15**, 372 (1972)].
[94] J. H. Towle and W. B. Gilboy, Nucl. Phys. **44**, 256 (1963).
[95] D. E. Bainum, R. W. Finlay, J. Rapaport, J. D. Carlson, and W. G. Love, Phys. Rev. C **16**, 1377 (1977).
[96] S. Tanaka, Y. Tomita, K. Ideno, and S. Kikuchi, Nucl. Phys. A **179**, 513 (1972).
[97] R. B. Galloway and J. Rahighi, Nucl. Instrum. Methods **297**, 452 (1990).
[98] J.-P. Jeukenne, A. Lejeune, and C. Mahaux, Phys. Rep. **25**, 83 (1976).
[99] J.-P. Jeukenne, A. Lejeune, and C. Mahaux, Phys. Rev. C **15**, 10 (1977).
[100] J. Berger, M. Girod, and D. Gogny, Comput. Phys. Commun. **63**, 365 (1990).
[101] A. Lejeune, Phys. Rev. C **21**, 1107 (1980).
[102] S. Goriely and J.-P. Delaroche, Phys. Lett. B **653**, 178 (2007).
[103] S. Péru and M. Martini, Eur. Phys. J. A **50**, 88 (2014).
[104] M. Blaizot and D. Gogny, Nucl. Phys. A **284**, 429 (1977).
[105] J. Dechargé and L. Šips, Nucl. Phys. A **407**, 1 (1983).
[106] J. W. Negele, Phys. Rev. C **1**, 1260 (1970).
[107] D. Gambacurta, F. Catara, M. Grasso, M. Sambataro, M. V. Andrés, and E. G. Lanza, Phys. Rev. C **93**, 024309 (2016).
[108] S. Goriely, S. Hilaire, M. Girod, and S. Péru, Phys. Rev. Lett. **102**, 242501 (2009).
[109] F. Chappert, N. Pillet, M. Girod, and J.-F. Berger, Phys. Rev. C **91**, 034312 (2015).
[110] D. Goutte, J. B. Bellicard, J. M. Cavedon, B. Frois, M. Huet, P. Leconte, P. X. Ho, S. Platchkov, J. Heisenberg, J. Lichtenstadt *et al.*, Phys. Rev. Lett. **45**, 1618 (1980).
[111] J. Heisenberg, J. Lichtenstadt, C. N. Papanicolas, and J. S. McCarthy, Phys. Rev. C **25**, 2292 (1982).
[112] D. Gogny, in *International Conference on Nuclear Physics, Munich,* edited by J. De Boer and H. J. Mang (North-Holland, Amsterdam, 1973), Vol. 1, p. 48.
[113] M. Dupuis, Ph.D. thesis, Université Bordeaux I, 2006, https://tel.archives-ouvertes.fr/tel-00412169.
[114] M. Dupuis, S. Karataglidis, E. Bauge, J.-P. Delaroche, and D. Gogny, Phys. Rev. C **73**, 014605 (2006).
[115] M. Dupuis, S. Karataglidis, E. Bauge, J.-P. Delaroche, and D. Gogny, Phys. Lett. B **665**, 152 (2008).
[116] M. Martin, Nucl. Data Sheets **108**, 1583 (2007).
[117] F. Kondev, Nucl. Data Sheets **109**, 1527 (2008).
[118] V. E. Starodubsky and N. Hintz, J. Phys. G **21**, 803 (1995).
[119] D. J. Horen, R. L. Auble, J. R. Beene, F. E. Bertrand, M. L. Halbert, G. R. Satchler, M. Thoennessen, R. L. Varner, V. R. Brown, P. L. Anthony *et al.*, Phys. Rev. C **44**, 128 (1991).
[120] D. J. Horen, C. L. Morris, S. J. Seestrom, F. W. Hersman, J. R. Calarco, M. Holtrop, M. Leuschner, M. Rawool-Sullivan, R. W. Garnett, S. J. Greene *et al.*, Phys. Rev. C **46**, 499 (1992).
[121] A. M. Mack, N. M. Hintz, D. Cook, M. A. Franey, J. Amann, M. Barlett, G. W. Hoffmann, G. Pauletta, D. Ciskowski, and M. Purcell, Phys. Rev. C **52**, 291 (1995).
[122] V. R. Brown, J. A. Carr, V. A. Madsen, and F. Petrovich, Phys. Rev. C **37**, 1537 (1988).
[123] C. N. Papanicolas, J. Heisenberg, J. Lichtenstadt, J. S. McCarthy, D. Goutte, J. M. Cavedon, B. Frois, M. Huet, P. Leconte, P. X. Ho *et al.*, Phys. Rev. Lett. **52**, 247 (1984).
[124] J. Coffin, N. Stein, T. Cleary, C. King, and D. Bromley, Nucl. Phys. A **181**, 337 (1972).
[125] A. Bernstein, V. Brown, and V. Madsen, Phys. Lett. B **103**, 255 (1981).
[126] Y. Wang and J. Rapaport, Nucl. Phys. A **517**, 301 (1990).
[127] P. E. Hodgson, *Direct Nuclear Reactions* (Clarendon, Oxford, UK, 1971).
[128] A. S. Meigooni, R. Finlay, J. Petler, and J. Delaroche, Nucl. Phys. A **445**, 304 (1985).
[129] S. Goriely, S. Hilaire, S. Péru, and K. Sieja, Phys. Rev. C **98**, 014327 (2018).
[130] J. Raynal, computer code ECIS06, NEA 0850/19, https://www.oecd-nea.org/tools/abstract/detail/nea-0850.
[131] P. Moldauer, Phys. Rev. C **14**, 764 (1976).
[132] P. Moldauer, Nucl. Phys. A **344**, 185 (1980).
[133] A. J. Koning, S. Hilaire, and M. Duijvestijn, in *Nuclear Data for Science and Technology*, edited by O. Bersillon, F. Gunsing,

E. Bauge, R. Jacqmin, and S. Leray (EDP Sciences, Les Ulis, France, 2008), p. 211.
[134] A. J. Koning and J.-P. Delaroche, Nucl. Phys. A **713**, 231 (2003).
[135] S. Shen, H. Liang, J. Meng, P. Ring, and S. Zhang, Phys. Rev. C **96**, 014316 (2017).
[136] C. Glashausser, D. L. Hendrie, and E. A. Mcclatchie, Nucl. Phys. A **222**, 65 (1974).
[137] G. Vallois, J. Saudinos, and O. Beer, Phys. Lett. B **24**, 512 (1967).
[138] J. Finck, G. Crawley, J. Nolen, and R. Kouzes, Nucl. Phys. A **407**, 163 (1983).
[139] T. Wood, Phys. Lett. B **46**, 41 (1973).
[140] N. L. Back and J. G. Cramer, Phys. Rev. C **28**, 1040 (1983).
[141] F. Perey and B. Buck, Nucl. Phys. **32**, 353 (1962).
[142] K. Amos, P. J. Dortmans, H. V. von Geramb, S. Karataglidis, and J. Raynal, Adv. Nucl. Phys. **25**, 275 (2000).
[143] H. F. Arellano and E. Bauge, Phys. Rev. C **84**, 034606 (2011).